A&A 487, 975–991 (2008)
DOI: 10.1051/0004-6361:200809426

Astronomy & Astrophysics

Modeling water emission from low-mass protostellar envelopes⋆

T. A. van Kempen[1], S. D. Doty[2], E. F. van Dishoeck[1,3], M. R. Hogerheijde[1], and J. K. Jørgensen[4]

[1] Leiden Observatory, Leiden University, PO Box 9513, 2300 RA Leiden, The Netherlands
e-mail: kempen@strw.leidenuniv.nl
[2] Department of Physics and Astronomy, Denison University, Olin 109 Granville, OH 43023, USA
[3] Max-Planck Institut für Extraterrestrische Physik (MPE), Giessenbachstr. 1, 85748 Garching, Germany
[4] Argelander-Institut für Astronomie, Universität Bonn, Auf dem Hügel 71, 53121 Bonn, Germany

Received 18 January 2008 / Accepted 3 April 2008

ABSTRACT

Context. Within low-mass star formation, water vapor plays a key role in the chemistry and energy balance of the circumstellar material. The Herschel Space Observatory will open up the possibility to observe water lines originating from a wide range of excitation energies.
Aims. Our aim is to simulate the emission of rotational water lines from envelopes characteristic of embedded low-mass protostars. A large number of parameters that influence the water line emission are explored: luminosity, density, density slope, and water abundances.
Methods. Both dust and water emission are modeled using full radiative transfer in spherical symmetry. The temperature profile is calculated for a given density profile. The H_2O level populations and emission profiles are in turn computed with a non-LTE line code. The results are analyzed to determine the diagnostic value of different lines, and are compared with existing observations.
Results. Lines can be categorized in: (i) optically thick lines, including ground-state lines, mostly sensitive to the cold outer part; (ii) highly excited (E_u > 200–250 K) optically thin lines sensitive to the abundance in the hot inner part; and (iii) lines which vary from optically thick to thin depending on the abundances. Dust influences the emission of water significantly by becoming optically thick at the higher frequencies, and by pumping optically thin lines.
Conclusions. A good physical model of a source, including the correct treatment of dust, is a prerequisite for inferring the water abundance structure and possible jumps at the evaporation temperature from observations. The inner warm (T > 100 K) envelope can be probed by highly excited lines, while a combination of excited and spectrally resolved ground state lines probes the outer envelope. Observations of $H_2^{18}O$ lines, although weak, provide even stronger constraints on abundances.

Key words. stars: pre-main sequence – circumstellar matter – stars: formation – ISM: molecules – submillimeter

1. Introduction

Low-mass (M < 3 $M_\odot$) young stellar objects (YSOs) form through gravitational collapse of cloud cores. Most of their mass is accreted over periods of less than 10^6 years (André et al. 2000; Myers et al. 2000). These early stages of low-mass star formation, the so-called Class 0 and Class I stages, are characterized by the presence of centrally condensed envelopes that veil the central protostars and disks (Lada 1987; André et al. 1993). The envelopes also contain most of the mass ($M \sim 0.1$–$1\ M_\odot$) of the total system until the emergence of the central star and disk (Adams et al. 1987; Shirley et al. 2000; Jørgensen et al. 2002). Water plays a pivotal role in these early evolutionary stages. First, the high dipole moment of H_2O makes its rotational lines excellent coolants of warm gas in the inner region of protostellar envelopes, allowing material to continue collapsing at higher temperatures (Goldsmith & Langer 1978; Neufeld & Kaufman 1993; Ceccarelli et al. 1996). Second, water is one of the dominant reservoirs of the non-refractory oxygen budget in dense clouds (van Dishoeck et al. 1993). The partitioning of gaseous oxygen between H_2O, OH and O, as well as the ratio between H_2O gas and ice, affect the chemistry of all other oxygen-containing molecules including the complex organics (Charnley et al. 1992). The evaporation point of H_2O ice in interstellar space is around 100 K (Fraser et al. 2001), so only the small warm inner regions of protostellar envelopes are likely to contain fractional abundances of water vapor as high as 10^{-4} with respect to H_2, perhaps even exceeding that of CO (e.g., Ceccarelli et al. 1996; van Dishoeck & Blake 1998; Boonman et al. 2003). In colder regions, water is the main ingredient of icy grain mantles as shown by infrared spectroscopy (e.g., Whittet et al. 1983; Smith et al. 1989; Boogert et al. 2002; Pontoppidan et al. 2004), with gas-phase water abundances that are orders of magnitudes lower. This abundance jump makes water an excellent tracer of warm, dense gas and a unique probe into the inner region close to the forming star.

Observations of interstellar gas-phase water from the ground are limited by the large amounts of water vapor in the Earth's atmosphere. Water maser lines at radio wavelengths longward of 3 mm (100 GHz), such as at 22 GHz, are readily seen, even from low-mass embedded YSOs (e.g., Furuya et al. 2003; Park & Choi 2007), but are constrained to small hot spots and are often variable in nature (Felli et al. 2007). They provide little information about the general physical and chemical evolution during star formation (Elitzur et al. 1989). One of the few exceptions of a non-masing water line observable from the ground is the 183 GHz $J = 3_{13}$–2_{02} transition, which can be used to trace widespread water emission under exceptional conditions

⋆ Figures 11–14 and Tables 9–12 are only available in electronic form at http://www.aanda.org

(e.g., Cernicharo et al. 1990, 1996; Doty 2000). Observations of deuterated water can also be done from the ground, in particular through the HDO 1_{01}–0_{00} 464 GHz, 3_{12}–2_{21} 225 GHz, and 2_{11}–2_{12} 241 GHz lines (e.g., Turner et al. 1975; Jacq et al. 1990; Helmich et al. 1996; Stark et al. 2004; Parise et al. 2005) and the D_2O 1_{10}–1_{01} 316 GHz line (Butner et al. 2007), but the large uncertainties in the D/H ratio owing to fractionation make such observations a poor tracer of water itself. The $H_2^{18}O$ isotopologue can be detected as well, but only through its high excitation temperature (E_{up} = 193 K) 3_{13}–2_{20} transition at 203 GHz (e.g., Jacq et al. 1988; Gensheimer et al. 1996; van der Tak et al. 2006).

To observe water emission lines systematically for a wide range of energy states, one has to turn to space-based observatories. Gaseous water has been detected in a number of star-forming regions using the Infrared Space Observatory (ISO), the Sub-millimeter Wave Astronomy Satellite (SWAS), and ODIN (e.g., Helmich et al. 1996; Harwit et al. 1998; Nisini et al. 1999; Ceccarelli et al. 1999; Snell et al. 2000; Bergin & Snell 2002; Maret et al. 2002; Nisini et al. 2002; Boonman et al. 2003; Bergin & Melnick 2005; Ristorcelli et al. 2005; Cernicharo & Crovisier 2005). However, due to large beams, low spectral resolution, or a combination of both, such observations were unable to accurately resolve the water abundance profile and trace the origin of the water emission, especially for low-mass YSOs. Two instruments onboard the Herschel Space Observatory[1] can be used for future observations of rotational water lines at unprecedented sensitivity, resolution and spectral coverage (Ceccarelli et al. 2001). The *Heterodyne Instrument for the Far Infrared* (HIFI) (de Graauw & Helmich 2001) and *Photodetector Array Camera and Spectrometer* (PACS) (Poglitsch et al. 2001) provide high spectral (up to 125 kHz) and spatial (20″ at 1 THz) resolution, which will allow a thorough analysis of water emission through a much wider range of observable transitions. In addition, the high sensitivity of the instrument will allow observations of various lines at low abundance, such as the optically thin isotopologues of water, in particular $H_2^{18}O$. However, to infer abundances from such observations, detailed radiative transfer calculations are needed.

Several modeling efforts have been carried out to analyze the observed water lines, based either on models of shocks at high and low velocities (e.g., Kaufman & Neufeld 1996; Giannini et al. 2001; Nisini et al. 2002) or on thermal emission from the envelope itself (e.g., Maret et al. 2002; Boonman et al. 2003). As pointed out by van der Tak et al. (2006), the high water abundance combined with its high dipole moment and its susceptibility to far-infrared emission from dust results in high optical depths make this molecule particularly difficult to model. As a result, no systematic parameter studies have been carried out yet We present here a parameter study of the water emission from low-mass protostellar envelopes using a full radiative transfer method including the effects of dust that is applied to realistic physical models of low-mass YSOs. Specific predictions for Herschel are made by convolving the computed emission with the Herschel observing beams. Poelman & van der Tak (2007) present similar models for high-mass protostars.

This paper is organized as follows. Section 2 presents the physical and molecular parameters necessary to accurately model water. Section 3 takes an in-depth look at a single Class 0 source, L 483, and explores the effects of possible water abundance profiles. Section 4 presents the results from the range of parameters that influence water emission. Section 5 investigates the influence of dust on water line fluxes and profiles, which is often ignored. Section 6 gives an analysis of a selected sample of observed water lines from ISO, SWAS, and ODIN to test the models and to infer implications for observations with future instruments such as HIFI and PACS. Final conclusions and recommendations can be found in Sect. 7.

[1] See http://herschel.esac.esa.int/

Table 1. Parameters for low-mass protostellar envelopes.

Variables	
n_{H_2}(1000 AU) (10^6 cm^{-3})	0.4, 1, 5
p	1.5, 2.0
Luminosity ($L_\odot$)	2, 7, 25
X_0 (water)	10^{-4}, 10^{-6}
X_d (water)	10^{-6}, 10^{-7}, 10^{-8}
Fixed parameters	
Distance	150 pc
Stellar temperature	5000 K
Gas temperature	$=T_{dust}$
R_{in} (inner radius)	250 K
R_{out} (outer radius)	200 R_{in}
r_0	1000 AU
Water freeze-out	100 K
o:p ratio H_2O[a]	3:1
o:p ratio H_2	1:1
Dust properties	OH 5[b]
Velocity dispersion ΔV	1.67 km s^{-1}

[a] For the L483 models, ortho-, and para-water were modeled independently. See Sect. 3; [b] see Ossenkopf & Henning (1994) Col. 5.

2. Model

The modeling has been carried out in two stages. First, the dust radiative transfer is calculated for a given power-law density profile (Sect. 2.1). This produces dust temperature profiles for given density structures. Subsequently, water level populations and line emission profiles are modeled using the line radiative transfer code RATRAN (Sect. 2.2) (Hogerheijde & van der Tak 2000), with the assumption that the gas temperature is equal to that of the dust. For an overview of the steps, see van Dishoeck (2003) (Fig. 2). Our method refers to the "empirical method" presented there. See Table 1 for an overview of the parameters.

2.1. Physical structure of the envelope model

2.1.1. Dust radiative transfer

Our protostellar envelope models are taken to be spherically symmetric, with the protostar located at the center. It has been shown that this assumption is valid for analyzing both the continuum and line emission down to scales of a few hundred AU (e.g., Shirley et al. 2000; Jørgensen et al. 2002; Schöier et al. 2002; Jørgensen et al. 2005). The density n at radius r within the protostellar envelope is described by

$$n(r) = n_0(r/r_0)^{-p}, \quad (1)$$

with the power-law exponent p and density n_0 at a reference radius r_0 as parameters. Within the context of protostellar collapse theories, both parameters depend on the age of the system and on the original core conditions, such as its initial mass.

Both the gas and dust temperatures inside the envelope are also often described by a power-law profile. However, this approximation fails at small radii where the dust becomes optically thick (e.g., Doty & Leung 1994; Jørgensen et al. 2002;

Table 2. The masses and inner radii of the model envelopes.

L_{bol} $L_\odot$	$n_{H_2}(r_0)$ 10^6 cm^{-3}	M_{env} $M_\odot$	R_{in} AU	$R_{100\ K}$ AU
		$p = 1.5$		
2	0.4	0.06	8.22	23
2	1	0.15	8.22	23
2	5	0.76	8.22	23
7	0.4	0.15	15.3	42
7	1	0.39	15.3	42
7	5	1.93	15.3	42
25	0.4	0.40	29	80
25	1	1.01	29	80
25	5	5.04	29	80
		$p = 2$		
2	0.4	0.07	8.22	21
2	1	0.18	8.22	21
2	5	0.90	8.22	21
7	0.4	0.13	15.3	38
7	1	0.33	15.3	38
7	5	1.65	15.3	38
25	0.4	0.24	29	72
25	1	0.63	29	72
25	5	3.15	29	72

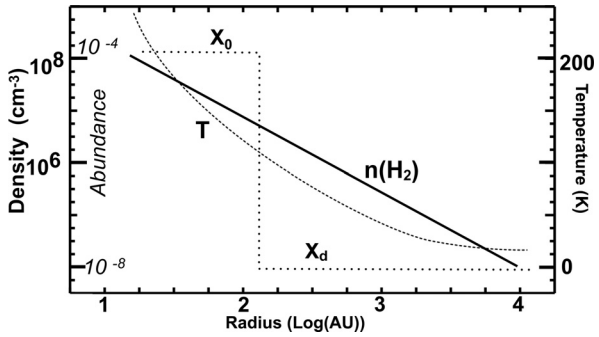

Fig. 1. Example of the physical structure of a model envelope with the density (solid), temperature (dashed), and abundance (dotted) displayed versus radius. The adopted parameters are $n_0(H_2) = 10^6$ cm^{-3}, $p = 1.5$, and $L = 2\ L_\odot$.

Young & Evans 2005). The actual temperature structure depends on a combination of the density structure and the central source luminosity, and a dust radiative transfer calculation is needed to determine it. The radiation is produced by the energy released through accretion of material onto the protostar.

The continuum radiative transfer through the envelope was calculated using the spherically symmetric dust radiative transfer code DUSTY (Ivezić & Elitzur 1997). DUSTY is a scale-free 1D code that uses the ratio Y of the outer over inner radius, R_{out}/R_{in}, the dust opacity τ at 100 μm, the temperature at R_{in}, and the power-law index of the density profile p as its variables. Results are then scaled by using the luminosity and distance of specific sources. The inner edge of our envelope R_{in} was set at the radius where the temperature of the envelope reaches 250 K. Material closer to the star is assumed to be located in a disk, which is not taken into account. In addition, we assume that the disk has no influence on the temperature and density distribution of the envelope. The exact inner radius in AU depends on the luminosity, which differs for each model, and R_{in} is typically a few tens of AU, much smaller than the Herschel beams (see Table 2). In all our models, Y is taken to be 200. Values of R_{out} are a few thousand to ten thousand AU, greater than the Herschel beam (20″ at 1113 GHz) at all but the lowest frequencies, but generally less than the values given in Jørgensen et al. (2002). The adopted dust opacity's are the often-used OH tables, Col. 5 of Ossenkopf & Henning (1994) throughout. Figure 1 shows a typical temperature and density profile.

2.1.2. Gas radiative transfer

The gas temperature is taken to be equal to the dust temperature for the entire spatial extent of our model, and the gas:dust mass ratio is taken to be 100:1. Warm dense gas can efficiently cool through the emission of excited molecular and atomic lines such as CO, H_2O, OH, and [O I] (Giannini et al. 2001). Water can also heat the gas through far-infrared pumping followed by collisional de-excitation (e.g., Ceccarelli et al. 1996). As a result, dust and gas temperatures can differ slightly, especially in the 100–200 K range (e.g., Ceccarelli et al. 2000; Maret et al. 2002); however, at densities of 10^7 cm^{-3} or higher, the gas and dust in the warm inner region couple efficiently. At low densities ($<10^5$ cm^{-3}) and temperatures (<50 K), any differences between gas and dust temperature depend on the source parameters (e.g., luminosity, total envelope mass) and the external interstellar radiation field (ISRF). Doty & Neufeld (1997) show in their Fig. 12 that these differences are generally small, about 10 K or less for low-mass YSOs, and typically only exist at radii greater than 2000 AU. Boonman et al. (2003) show that for high-mass YSOs, the water line emission for a full radiative transfer calculation of the gas temperature differs negligible from that calculated using the $T_{dust} = T_{gas}$ assumption.

Our choice of $R_{out} = 200\ R_{in}$ assumes that water vapor at larger radii does not contribute to the total water line emission due to the low densities ($<10^5$ cm^{-3}) and temperatures (<15 K) in these regions. This assumption mostly affects the transitions leading to the ground states. Any such material is able to absorb water emission for optically thick lines, and lead to weak emission lines in observations taken with a beam that is much larger than our adopted source sizes. However, such extended envelope material is almost indistinguishable from any larger scale cloud complexes not directly related to the source. Such contributions from large-scale clouds need to be taken into account on a source-by-source basis, but are beyond the scope of this work. The protostellar envelopes are assumed to be shielded from strong external radiation fields by surrounding molecular cloud material. If directly exposed to outside radiation, the temperature in the outer envelopes is affected by the ISRF, but material is not heated by more than 40 K for the ISRF found within the Orion starforming region (Jørgensen et al. 2006). Low-mass starforming regions are expected to have significantly lower ISRF. External radiation is not considered for these models.

2.1.3. Grid parameters

To limit the model complexity, the wide range of parameters was reduced to four variables (see Table 1). The density at 1000 AU, $n_0(H_2)$ and the exponent of the density power law p are two of these. Jørgensen et al. (2002) observed many low-mass YSOs and inferred densities at 1000 AU between 1×10^5 to 5×10^6 cm^{-3}. Accordingly, three values, 0.4×10^6, 1×10^6, and 5×10^6 cm^{-3} were chosen to sample this range, and p was chosen to be either 1.5 or 2.0. The stellar variables are reduced to a single variable, the luminosity. Models using luminosities of 2, 7, and 25 $L_\odot$ are explored to represent the wide range of luminosities observed in low-mass protostars. Although the

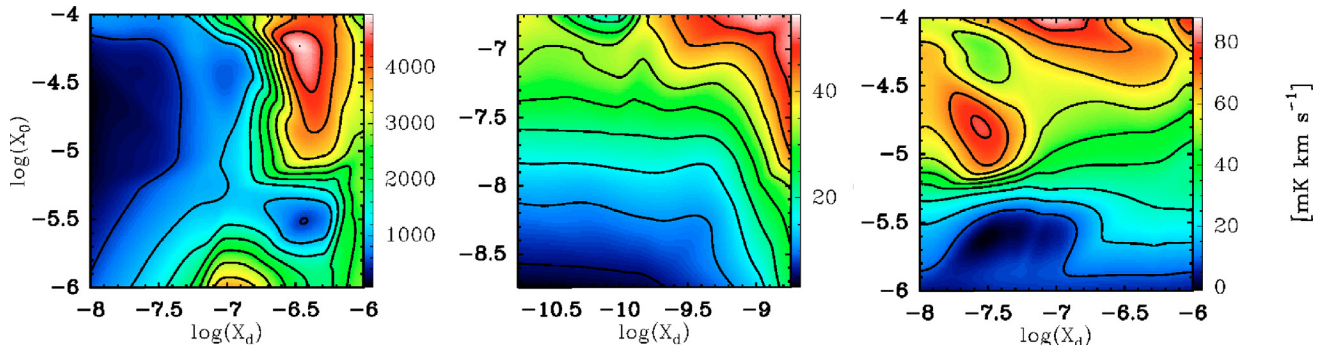

Fig. 2. Contour plots of the integrated water line intensity for the L 483 models, plotted as functions of X_d and X_0. *Left*: the o-H_2O 1_{10}–1_{01} line (557 GHz), showing a strong dependence on X_d; *middle*: the p-$H_2^{18}O$ 2_{02}–1_{11} line (995 GHz), showing a clear cut between the dependency on X_d or X_0, depending on the abundance profile; *right*: the p-H_2O 5_{24}–4_{31} line (970 GHz), showing a strong dependence on X_0.

surface temperature of the protostar cannot be derived directly, it is assumed to be around 5000 K for low-mass young stars, regardless of the luminosity or age. Test models show that, due to the reprocessing of stellar photons into IR/thermal photons very close to the star, the stellar effective temperature has little influence on the modeling. The final variable is the gas-phase water abundance, to be discussed below. Table 1 summarizes all the adopted parameters. The resulting masses and inner and outer radii for each envelope model can be found in Table 2.

2.2. H_2O line modelling

Because of the gradient in temperature, the water abundance X with respect to H_2 is expected to vary within YSO envelopes. Previous studies of low- and high-mass YSOs used a variety of H_2O observations with ISO-LWS, ISO-SWS, and/or SWAS to constrain the water abundance profile in protostellar envelopes to have a "jump" in abundance at a characteristic temperature around 100 K (e.g., Maret et al. 2002; Boonman et al. 2003; van der Tak et al. 2006). Such "jumps" have also been confirmed by ground-based observations of other molecules such as CH_3OH and H_2CO (e.g., van der Tak et al. 2000; Ceccarelli et al. 2000; Schöier et al. 2002; Jørgensen 2004; Maret et al. 2004). The abundance of water in the inner region X_0 is high for two reasons. First, most water exists in the gas phase above 100 K, the temperature at which water ice evaporates from the grains. Second, gas-phase reactions of atomic oxygen with molecular hydrogen drive all oxygen into water at high temperatures ($T > 230$ K) (Charnley et al. 2001). However, in regions where the temperature drops below 100 K, water is mostly frozen out onto the grains, and only trace amounts of gaseous water are present with an abundance X_d.

Accordingly, "jump" abundances are assumed for all models with X_0, the abundance of the warm inner region, taken to be 10^{-4} or 10^{-6} , and X_d, the abundance in the cold outer region, taken to be 10^{-6}, 10^{-7}, or 10^{-8}. These values cover the range of inferred abundances from observations to date for embedded protostars. Although beam-averaged H_2O abundances below 10^{-8} have been observed for B 68 and Oph-D (Bergin & Snell 2002), such clouds are starless. At the extremely low temperatures of <15 K, virtually all heavy elements are frozen out. Abundances as low as 10^{-11} were tested by Boonman et al. (2003), but models with outer abundances of 10^{-8} were preferred in fitting the combined SWAS and ISO-LWS data. One combination of abundances is a constant abundance at 10^{-6}, included to investigate the differences between "jump" and constant abundance profiles. A finer grid of abundances within this range is explored for the L 483 model. Figure 1 includes the assumed abundance structure. Our models do not consider a so-called "drop" abundance profile (see Schöier et al. 2004), in which the abundance in the outermost part is higher due to longer timescales for freeze-out at lower densities and due to photodesorption of ices (Bergin & Melnick 2005). Such an abundance profile would result in more self-absorption in the ground-state lines, equivalent to absorption caused by the cold fore-ground material not associated with the protostellar system.

The effects of micro-turbulence within the envelope are represented by a velocity dispersion $FWHM$, $\Delta V = 1.67\ \mathrm{km\,s^{-1}}$ ($b = 1\ \mathrm{km\,s^{-1}}$, with b the Doppler parameter), consistent with the typical line widths observed for optically thin rotational emission in low-mass YSO envelopes (Jørgensen et al. 2002, 2004, 2005). For a more thorough discussion of the effects of the choice of this value, see Sect. 5.2. An infall velocity profile was included, based on the velocity profiles for collapsing clouds as found by Shu (1977). This velocity profile was scaled to a velocity of 4 km s^{-1} at the inner radius R_{in}. At radii of a few hundred AU, the micro-turbulent velocity dominates over the infall velocity, which is the scale probed mostly by single-dish observations (e.g., Jørgensen et al. 2004). H_2 is assumed to be in a 1:1 ortho to para ratio. Water itself is in 3:1 ortho to para ratio. Collisional rate coefficients for both ortho- and para-H_2O with ortho- and para-H_2 were obtained from the LAMDA database (Schöier et al. 2005) based on calculations by Green et al. (1993) for temperatures in the range from 20 to 2000 K. New rate coefficients have recently been published (Phillips et al. 1996; Dubernet & Grosjean 2002; Grosjean et al. 2003; Faure et al. 2007)[2]. For a general discussion of uncertainties in molecular data, see Schöier et al. (2005).

The excitation and radiative transfer of the rotational water lines were calculated using the spherically symmetric version of the RATRAN code (Hogerheijde & van der Tak 2000). First, level populations were computed for all H_2O levels with energies up to 2000 K for the model envelope using full Monte Carlo radiative transfer. Individual iterations use a convergence criterion

[2] The rate coefficients from Faure et al. (2007) only became available once most of the models had been run, but those new calculations often do not include a wide enough range of temperatures or the higher excited energy levels, needed for the analysis of YSOs. Test models using different published rate coefficients show that absolute line fluxes may differ up to 30% (Poelman & van der Tak 2007). Even greater differences are found at low temperatures ($T < 20$ K) and densities ($n(H_2) < 10^4$ cm^{-3}) for the ground-state line intensities and profiles (e.g. Poelman & Spaans 2005; Dubernet et al. 2006). However, the general trends found in this paper remain valid for different rate coefficients.

Table 3. Key water lines observable with Herschel HIFI and PACS.

Transition	Freq. (GHz)	Wavelength (μm)	E_{up} (K)	Beam[a] ($''$)
HIFI				
Ortho-H_2O transition				
1_{10}–1_{01}	556.93607	538.66147	61.0	39
2_{12}–1_{01}	1669.90496	179.65094	114.4	13
2_{21}–2_{12}	1661.00802	180.61322	194.1	13
3_{12}–2_{21}	1153.12682	260.16219	249.4	19
3_{12}–3_{03}	1097.36505	273.38213	249.4	21
3_{21}–3_{12}	1162.91187	257.97312	305.3	19
Para-H_2O transition				
1_{11}–0_{00}	1113.34306	269.45872	53.4	21
2_{02}–1_{11}	987.92670	303.66625	100.8	21
2_{11}–2_{02}	752.03323	398.91854	136.9	30
2_{20}–2_{11}	1228.78902	244.14281	195.9	19
3_{31}–4_{04}	1893.68681	158.42113	410.4	13
4_{22}–3_{31}	916.17164	327.44956	454.3	25
4_{22}–4_{13}	1207.63890	248.41863	454.3	19
5_{24}–4_{31}	970.31524	309.17787	598.8	21
PACS				
Ortho-H_2O transition				
2_{12}–1_{01}	1669.90496	179.65094	114.4	13
2_{21}–1_{10}	2773.97691	108.14798	194.1	8
2_{21}–2_{12}	1661.00802	180.61322	194.1	13
3_{03}–2_{12}	1716.76979	174.74678	196.8	12
4_{14}–3_{03}	2640.47434	113.61595	323.5	8
Para-H_2O transition				
2_{20}–1_{11}	2968.74895	101.05267	195.9	7
3_{13}–2_{02}	2164.13230	138.62371	204.7	10
4_{04}–3_{13}	2391.57290	125.44046	319.5	9

[a] Taken from http://herschel.esac.esa.int/home.shtml

of 10^{-6} on the relative error of the fractional population for the solution of the statistical equilibrium. Iterations continue with increasing amounts of photons, until the greatest relative difference between fractional populations over all cells and all levels of three subsequent iterations is less than 1/6. In practice this means that the vast majority of cells and levels are converged to much smaller relative errors. Far-infrared radiation from the dust and CMB are included in the H_2O excitation and line formation. This inclusion makes it possible to investigate infrared pumping, self-absorption of a line, and absorption against the dust continuum. Even though many levels are very sparsely populated, tests show that it is necessary to include the higher levels to obtain an accurate population distribution throughout the model.

The populations are then used to reconstruct detailed line profiles through ray-tracing, which can be convolved with any beam or area. It can also be used to make velocity maps of the source. The adopted spectral resolution is 0.05 km s^{-1}. RATRAN was benchmarked against many codes (van Zadelhoff et al. 2002). Furthermore, it was part of a recent benchmark test[3] for line modeling of H_2O (van der Tak et al. 2005).

Although level populations were calculated for all levels up to E_{up} = 2000 K, only lines with an upper energy level below 500 K were selected for the presentation of results (see Table 3). Both H_2O and $H_2^{18}O$ were modeled with a focus on lines that fall into the Herschel wavelength range. The ^{16}O:^{18}O isotope ratio was assumed to be 550:1, the ratio in the local ISM (Wilson & Rood 1994). All generic models are placed at 150 pc, the typical distance of most nearby low-mass starforming regions such as Ophiuchus, Taurus, and Chameleon. Results were convolved with the appropriate Herschel beams and given in main beam temperatures. For reference, the typical sensitivities expected with HIFI (5σ, 0.5 h, 0.5 km s^{-1} resolution) are 60 mK for 557 GHz, 180 mK at 1130 GHz, and 600 mK at 1669 GHz. For PACS, limiting line fluxes (5σ, 0.5 h, point source) range from 6×10^{-18} W m^{-2} to 35×10^{-18} W m^{-2} [4]. To convert from main beam temperatures T_{MB} to fluxes S_ν in Jy (10^{-26} W m^{-2} Hz^{-1}), use the formula

$$S_\nu = 2.65 \times 10^8 \times T_{MB}(\mathrm{K}) \times \theta_0^2(') \times \lambda^{-2}(\mu\mathrm{m}). \quad (2)$$

This assumes a source size equivalent to the beam size. For sources smaller than the beam, a correction needs to be taken into account. The Herschel beam θ_0 ranges from 40$''$ (0.66$'$) at 557 GHz (539 μm) to 7$''$ (0.12$'$) at 3000 GHz (100 μm) (see Table 3).

3. Example: L 483

3.1. Physical structure

As an illustrative model, the isolated Class 0 source L 483, (Motte & André 2001) located at 200 pc, was modeled to investigate the sensitivity of the water line intensities to different abundances. This source has been studied extensively by Jørgensen et al. (2002) and Jørgensen (2004) and its physical and chemical structure is well-constrained through continuum and line data from (sub)millimeter single-dish telescopes and interferometers. The well-determined envelope and source parameters (L_{bol} = 9 $L_\odot$ and $n_0(H_2) = 1 \times 10^6$ cm^{-3}) are roughly in the middle of our parameter range, making L 483 an excellent test-case for modeling water emission. Only the inferred density slope, p = 0.9, is somewhat flatter than for other sources, but this does not influence the model trends. For CO, a jump abundance at an evaporation temperature of $T \approx 30$ K was found to explain the observed molecular lines. Any compact disk is constrained to a mass of 0.012 $M_\odot$ using interferometer observations with the Sub-Millimeter Array (Jørgensen et al. 2007), negligible compared to the total estimated envelope mass of 4.4 $M_\odot$ out to the 10 K radius of 10 000 AU. In addition, this source has been observed with ISO-LWS (Giannini et al. 2001). The best-fit parameters from the dust radiative transfer (Y = 1400, p = 0.9, τ_{100} = 0.3), which fit both the SED and the spatial extent of the SCUBA continuum data, determine the physical structure of the envelope. R_{in} (at T = 250 K) is 9.9 AU for this rather shallow density profile, and R_{out} is ~10 000 AU. The radius where water freezes out onto the grains (T = 100 K) is located at 35 AU. This L 483 model was used to explore a wider variety of water abundances than the generic models. Specifically, values of $1 \times 10^{-4}, 5 \times 10^{-5}, 1 \times 10^{-5}, 5 \times 10^{-6}$, and 1×10^{-6} were used for X_0 and $1 \times 10^{-6}, 5 \times 10^{-7}, 1 \times 10^{-7}, 5 \times 10^{-8}$, and 1×10^{-8} for X_d. All other parameters were kept fixed. Ortho- and para-water were modeled separately, and water abundances are given for ortho- or para-water individually instead of the combined total water abundance with the used 3:1 ortho to para ratio. This allows independent probes of the ortho to para ratio. Thus, X_0 and X_d refer to either ortho- or para-H_2O, depending on the line in question.

3.2. Results

In Table 4 the integrated emission of both $H_2^{16}O$ and $H_2^{18}O$ lines, observable with Herschel-HIFI (see Table 3), are presented for

[3] See http://www.sron.rug.nl/~vdtak/H2O/

[4] Calculated with Hspot, see http://herschel.esac.esa.int/

Table 4. Integrated intensities, $\int T_{\rm MB} dV$ [K km s^{-1}], for H_2O and $H_2^{18}O$ lines for L 483 models with various abundances. Negative values indicate strong (self-) absorbed lines.

Transition	$X_0 = 10^{-4}$			$X_0 = 10^{-5}$			$X_0 = 10^{-6}$		
X_d =	10^{-6}	10^{-7}	10^{-8}	10^{-6}	10^{-7}	10^{-8}	10^{-6}	10^{-7}	10^{-8}
Ortho-H_2O transitions									
1_{10}–1_{01}	2.7	2.4	0.83	2.8	1.0	8.8(–2)	9.5	3.8	0.57
2_{12}–1_{01}	–0.2	–0.13	0.27	–0.35	–0.38	–0.33	3.0	0.23	–0.05
2_{21}–2_{12}	1.7	0.27	0.20	0.17	0.32	0.11	1.7	0.37	0.12
3_{12}–2_{21}	0.8	0.17	0.10	0.47	0.12	7.8(–2)	0.95	0.20	7.1(–2)
3_{12}–3_{03}	0.8	0.29	0.13	0.43	0.22	6.0(–2)	0.94	0.39	7.4(–2)
3_{21}–3_{12}	1.3	0.35	0.11	0.73	0.26	5.4(–2)	1.5	0.46	8.2(–2)
Para-H_2O transitions									
1_{11}–0_{00}	–6.5(–3)	1.23	–0.17	–0.12	5.2(–2)	0.29	3.12	1.4	–0.13
2_{02}–1_{11}	1.1	0.59	0.26	1.4	0.6	0.45	0.6	1.4	0.26
2_{11}–2_{02}	0.85	0.73	0.16	0.99	0.6	0.34	0.96	1.1	0.15
2_{20}–2_{11}	0.38	0.61	0.18	0.45	0.50	0.31	0.38	0.83	0.13
3_{31}–4_{04}	4.4(–2)	6.3(–2)	6.3(–2)	1.9(–2)	1.9(–2)	2.7(–2)	3.7(–3)	1.9(–3)	1.3(–3)
4_{22}–3_{31}	5.0(–2)	6.8(–2)	3.7(–2)	5.2(–2)	5.6(–2)	5.1(–2)	1.8(–2)	1.5(–2)	9.7(–3)
4_{22}–4_{13}	0.21	8.6(–2)	5.3(–2)	0.25	8.3(–2)	8.0(–2)	0.24	0.10	5.8(–3)
5_{24}–4_{31}	6.0(–2)	8.8(–2)	5.5(–2)	3.2(–2)	4.3(–2)	5.5(–2)	4.0(–3)	5.9(–3)	3.3(–3)
Ortho-$H_2^{18}O$ transitions									
1_{10}–1_{01}	–3.3(–2)	–5.6(–3)	2.3(–2)	–4.0(–2)	–2.0(–2)	5.2(–3)	–1.9(–2)	–2.4(–2)	–3.9(–4)
2_{12}–1_{01}	–0.13	–3.3(–2)	1.2(–2)	–0.13	–4.5(–2)	–6.7(–4)	–0.12	–4.9(–2)	–5.2(–3)
2_{21}–2_{12}	4.1(–3)	4.2(–3)	3.7(–3)	1.8(–3)	9.6(–4)	9.3(–4)	1.0(–3)	1.3(–4)	1.1(–4)
3_{12}–2_{21}	5.6(–2)	6.0(–2)	5.9(–2)	3.6(–3)	3.0(–3)	3.0(–3)	5.9(–4)	1.39(–4)	1.2(–4)
3_{12}–3_{03}	2.5(–2)	2.6(–2)	2.5(–2)	8.5(–3)	6.9(–3)	6.8(–3)	2.0(–3)	4.6(–4)	3.8(–4)
3_{21}–3_{12}	1.7(–2)	1.9(–2)	1.8(–2)	4.5(–3)	3.6(–3)	3.5(–3)	1.0(–3)	2.1(–4)	1.7(–4)
Para-$H_2^{18}O$ transitions									
1_{11}–0_{00}	–0.21	–7.7(–2)	8.7(–3)	–0.16	–8.8(–2)	–4.7(–3)	–0.21	–9.3(–2)	–1.2(–2)
2_{02}–1_{11}	5.3(–2)	4.0(–2)	3.8(–2)	4.4(–2)	2.0(–2)	1.8(–2)	2.5(–2)	4.7(–3)	3.1(–3)
2_{11}–2_{02}	2.5(–2)	1.9(–2)	1.9(–2)	2.0(–2)	7.9(–3)	7.6(–3)	9.6(–3)	1.5(–3)	1.1(–3)
2_{20}–2_{11}	1.7(–2)	1.4(–2)	1.4(–2)	1.6(–2)	6.5(–3)	6.2(–3)	7.2(–3)	1.0(–3)	6.9(–4)
3_{31}–4_{04}	9.2(–5)	1.2(–4)	1.2(–4)	5.7(–6)	4.6(–6)	4.6(–6)	5.1(–7)	2.5(–7)	2.3(–7)
4_{22}–3_{31}	6.3(–4)	8.4(–4)	8.5(–4)	2.8(–5)	2.3(–5)	2.3(–5)	9.1(–7)	6.7(–7)	6.4(–7)
4_{22}–4_{13}	2.5(–2)	3.0(–2)	3.0(–2)	1.5(–3)	1.2(–3)	1.2(–3)	4.8(–5)	3.5(–5)	3.4(–5)
5_{24}–4_{31}	7.1(–5)	1.1(–4)	1.1(–4)	1.6(–6)	1.3(–6)	1.3(–6)	4.6(–8)	4.2(–8)	4.0(–8)

In this and subsequent tables, the notation $A(B)$ indicates $A \times 10^B$.

the reference grid of L 483, whereas Table 5 presents the peak temperatures. Detailed contour plots of all HIFI lines as functions of X_0 and X_d are presented in Fig. 2 the online appendix. Many of the trends discussed below are similar to those found for AFGL 2591, as discussed in Poelman & van der Tak (2007). Overall, lines are found to belong to three categories. First, all excited $H_2^{18}O$ and several H_2O highly excited ($E_{up} > 200$ K) lines are completely optically thin. They have Gaussian profiles with widths that depend on the turbulent width. Due to the freeze-out of water onto grains below 100 K, these optically thin lines probe the inner warm dense region. For the model where water has a constant abundance of 10^{-6}, emission from the warm dense inner region still dominates and is optically thin (either due to the low population of the highly excited states or the low abundance of $H_2^{18}O$). A good example is the H_2O 5_{24}–4_{31} 970 GHz line shown in Fig. 2 (*right*).

The ground state lines of both $H_2^{18}O$ and H_2O, together with most H_2O excited lines with energies below 200 K, provide a strong contrast with the optically thin lines. These lines only probe the outer region. Even an abundance of water as low as 10^{-8} in the cold outer envelope produces a high enough column for these lines to become optically thick. The extremely high optical depth ($\tau > 25$) and the absorptions into the dust further prevent the integrated intensity from probing the entire envelope. Thus, these lines trace the outer abundance X_d, and self-absorption and absorption of the dust continuum are commonly found in their line profiles. However, most optically thick lines have wings that are either optically thin or less optically thick. These wings may be able to probe the inner region up to the boundary layer around $T = 100$ K. See the 1_{10}–1_{01} line in Fig. 2 (*left*), Table 5 and the spectra in Figs. 3 and 4 (discussed in Sect. 3.4).

Finally, some lines are optically thick for a high X_0–X_d combination, but are optically thin at low abundances. It is not known a-priori if these lines originate within the cold outer envelope or the warm dense inner regions. Examples are several of the highly excited H_2O lines, but such dependencies are also seen for lowly excited $H_2^{18}O$ lines. Figure 2 (*middle*) shows an example with the p-$H_2^{18}O$ 2_{02}–1_{11} line. It can be seen that, depending on the total column of water, this line either traces X_d at high columns or X_0 at lower columns. For the $H_2^{18}O$ lines, a clear dividing line between dependency on X_0 or X_d lies at $X_d(H_2^{18}O) < 10^{-9.5}$ (see online appendix). Such a division is less clear for $H_2^{16}O$. The dust can become optically thick, especially at high frequencies, so the higher frequency lines will not be able to probe the inner region at all. For the L 483 models, this only takes place at frequencies higher than 1500 GHz, but see Sect. 5 for further discussion. In the following, individual H_2O and $H_2^{18}O$ lines are discussed in more detail.

Table 5. Peak temperatures [K] of H_2O lines for L 483 models of various abundances. Negative values primarily indicate absorption into the dust continuum.

Transition	$X_0 = 10^{-4}$			$X_0 = 10^{-5}$			$X_0 = 10^{-6}$		
X_d =	10^{-6}	10^{-7}	10^{-8}	10^{-6}	10^{-7}	10^{-8}	10^{-6}	10^{-7}	10^{-8}
Ortho-H_2O transitions									
1_{10}–1_{01}	2.8	2.1	0.65	2.8	1.1	0.2	5.4	2.8	0.5
2_{12}–1_{01}	0.45	0.35	0.25	0.3	–0.13	–0.13	1.9	–0.13	0.25
2_{21}–2_{12}	1.1	0.1	0.05	0.2	0.1	3.8(–2)	1.6	0.21	4.5(–2)
3_{12}–2_{21}	0.28	6.5(–2)	2.4(–2)	0.18	4.5(–2)	2.1(–2)	0.36	0.1	2.4(–2)
3_{12}–3_{03}	0.27	0.12	4.1(–2)	0.12	0.1	1.5(–2)	0.4	0.17	2.8(–2)
3_{21}–3_{12}	0.5	0.18	4.1(–2)	0.33	0.13	1.5(–2)	0.55	0.26	3.2(–2)
Para-H_2O transitions									
1_{11}–0_{00}	1.5	1.3	–9(–2)	0.45	0.45	0.45	1.6	1.25	0.13
2_{02}–1_{11}	1.6	0.55	8(–2)	1.1	0.4	0.18	0.9	1.0	8(–2)
2_{11}–2_{02}	0.8	0.22	7(–2)	0.38	0.18	0.16	0.45	0.38	7.5(–2)
2_{20}–2_{11}	0.4	0.28	7.5(–2)	0.12	0.24	0.17	0.1	0.35	7(–2)
3_{31}–4_{04}	2.8(–2)	2.2(–2)	2.2(–2)	1(–2)	1(–2)	1.9(–2)	2.5(–3)	1.5(–3)	8(–4)
4_{22}–3_{31}	2.8(–2)	2(–2)	1(–2)	2.3(–2)	2.4(–2)	1.5(–2)	1.2(–2)	1(–2)	6(–3)
4_{22}–4_{13}	0.16	2.4(–2)	1.4(–2)	0.12	2.7(–2)	1.7(–2)	0.12	4.5(–2)	2.2(–2)
5_{24}–4_{31}	2.2(–2)	2.6(–2)	1.6(–2)	1.8(–2)	1.9(–2)	2.4(–2)	2.5(–3)	3.5(–3)	2(–3)

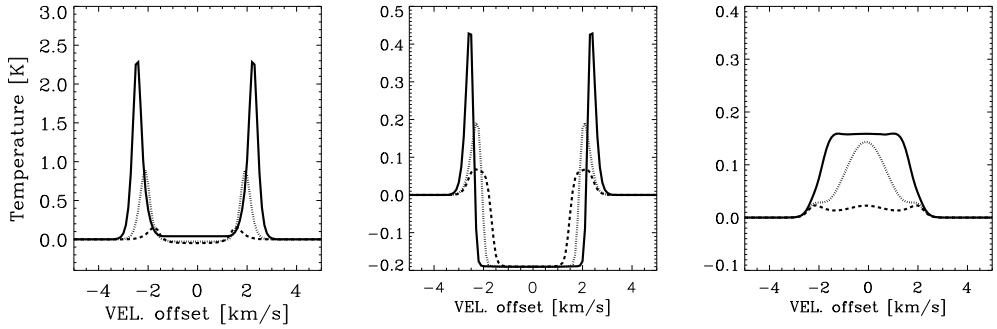

Fig. 3. H_2O spectra for an abundance X_0 of 10^{-5} for the 1_{10}–1_{01} (557 GHz, *left*), 2_{12}–1_{01} (1669 GHz *middle*), and 3_{12}–3_{03} (1097 GHz *right*) lines. Lines are shown for X_d of 10^{-6} (solid), 10^{-7} (dot), and 10^{-8} (dash).

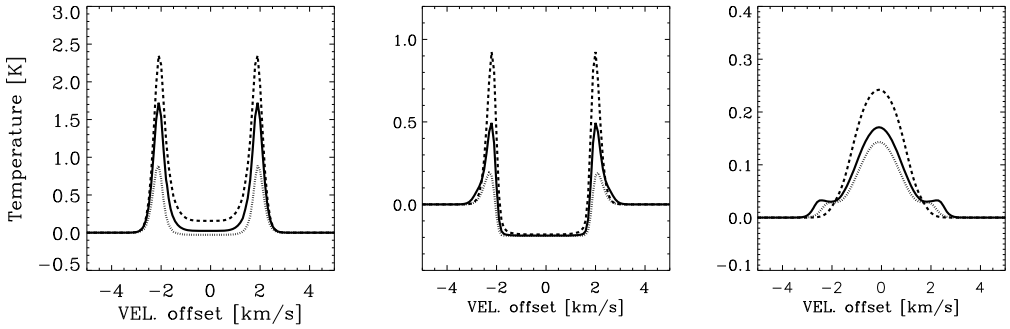

Fig. 4. H_2O spectra for an abundance X_d of 10^{-7} for the 1_{10}–1_{01} (557 GHz *left*), 2_{12}–1_{01} (1669 GHz *middle*), and 3_{12}–3_{03} (1097 GHz *right*) lines. Lines are shown for X_0 of 10^{-4} (solid), 10^{-5} (dot), and 10^{-6} (dash).

3.3. Integrated emission

3.3.1. H_2O

The main isotopologue of water, $H_2^{16}O$, is optically thick in most transitions considered here. All lines with $J_{up} = 1$ and 2 are optically thick and trace the outer cold envelope. Most other lines trace either the warm inner or cold outer envelope. The integrated intensities of these "hybrid" lines depend sensitively on the precise abundance parameters of the L 483 reference model. In particular, the radius where the line turns optically thick is comparable to that where the one where the temperature reaches 100 K for this model. These are the 2_{21}–2_{12}, 3_{12}–2_{21}, 3_{12}–3_{03}, 3_{21}–3_{12} and 4_{22}–4_{13} lines. At low abundances of X_d, they depend more on X_0. If the abundance in the outer region is larger than 5×10^{-8}, they depend on X_d instead. The integrated intensities range from several hundreds of mK km s^{-1} in absorption to a few K km s^{-1} in emission, with peak brightness from 100 mK to 1 K, readily detectable with HIFI. The group of highly excited para-lines have peaks up to a few tens of mK, requiring much longer integration times.

Dependencies of the line strengths on abundances are not linear. An exception is whenever the line is completely optically

thin over the entire profile. This is not the case for most lines and parts of the line profile will be optically thin and parts optically thick, causing complicated dependencies. For instance, the total integrated intensity of the 557 GHz line depends sensitively on the inner and outer abundances. Abundance combinations of $10^{-4}/10^{-6}$ produce lines with less total emission than $10^{-6}/10^{-6}$. The $10^{-6}/10^{-6}$ combination contains less water emission originating from the warm inner regions, but more dust continuum is able to escape the inner regions in the $10^{-6}/10^{-6}$. This influences the population distribution in the outer region, resulting in less central absorption. Since absorption is a major feature within this line profile, the total integrated line intensity effectively goes up.

3.3.2. $H_2^{18}O$

Because of the low abundance of the $H_2^{18}O$ isotopologue, most of its lines are optically thin. Only the three transitions connecting to the ground levels of ortho- and para-$H_2^{18}O$ – 1_{11}–0_{00}, 1_{10}–1_{01}, and 2_{12}–1_{01} – have optical depths higher than 5 for all abundances. However, excited lines with $J_{up} = 2$ are optically thick in their line centers for $X_0 > 10^{-5}$. The integrated intensities of these $H_2^{18}O$ lines range from a few hundred mK km s^{-1} in absorption to a few tens of mK km s^{-1} in emission, whereas peak temperatures range from a few mK to a few tens of mK, thus requiring long integration times. Due to the low abundance, the dependence on either X_0 or X_d is much more evident than for $H_2^{16}O$ (see Fig. 2 for example). The optically thick ground-state lines accurately trace X_d, while optically thin excited lines only depend on X_0. The few optically thick excited lines trace X_0 as well, since the $\tau = 1$ surface lies within the 100 K radius. Higher excitation $H_2^{18}O$ lines are not very strong, in the range of a few micro-K to a few milli-K, too weak to be detectable with HIFI in reasonable integration times.

3.4. Line profiles

A number of characteristic line profiles are presented in Figs. 3 and 4. The continuum has been subtracted so that the profiles can be readily compared on the same scale. The total profile contains valuable information about the envelope structure and velocity profile, none of which can be determined using the integrated line intensity alone. As seen in the examples, there is a wide variety of model profiles depending on a number of parameters. First, the excitation energy of the upper state, the total water column density and the critical density of the line in question will determine whether an emission line is optically thick, thin or a combination of both. Most lines show a combination, with optically thin wings around an optically thick line center. Second, the width depends on the systematic and turbulent velocity. Third, water in the colder outer envelope will absorb photons and scatter the radiation, causing an absorption feature. Finally, the optical depth of dust itself blocks line emission at frequencies above 1500 GHz originating in the inner region. In the following these profile shapes are discussed in more detail.

The profiles of optically thin lines are Gaussian and are good tracers of the velocity profile. Optically thin lines always trace the inner warm region, where the higher excitation states are populated. The ratio of the line wing over the peak temperature can vary, depending on the excitation energy of the line. Higher excitation lines are broader, while low excitation lines have a narrower peak with very weak line wings. An example in Fig. 4 is the 3_{12}–3_{03} 1097 GHz line, which is completely optically thin for $X_0 = 10^{-6}$. The line center becomes optically thick at $X_0 = 10^{-5}$ and thus decreases, but the optically thin line wings are noticeably higher in emission. At $X_0 = 10^{-4}$, the optically thick line center is brighter than at 10^{-5} due to the high abundance, but still weaker than the optically thin emission at $X_0 = 10^{-6}$.

The profiles of optically thick lines are much more complicated. Their wings can either be optically thick or thin, depending on the abundances and frequency of the line. This gives rise to three different profiles.

- Lines with a Gaussian line center, but with enhanced line wings. A characteristic "bump" can be seen at velocities where the line profile changes from optically thick to thin when going to more extreme velocities. The line center is optically thick, but is heavily pumped by the line radiation coming from water in the warmer regions further inwards in the envelope. This behavior is often called "effectively optically thin". Such lines trace the inner abundance X_0, unless optically thick dust veils the inner region. An example is seen by the 3_{12}–3_{03} 1097 GHz line with an X_0 of 10^{-4} in Fig. 4.
- "Flat top" lines, where the center of the line is optically thick, but not self-absorbed. The center of the line is dominated by emission from a small region with a specific temperature. Line wings are optically thin. Material at larger radii is unable to cause self-absorption, and there is not enough material deeper within the envelope to make such a line "effectively optically thin". Optically thick dust can prevent warmer regions from influencing the line at higher frequencies. An example is given by the 3_{12}–3_{03} 1097 GHz line with $X_d = 10^{-6}$ in Fig. 3.
- Deeply (self)-absorbed lines with most of the emission in the line wings. Absorption into the dust occurs, and is stronger for high frequency lines, where the dust continuum is higher. All three ground state lines show such profiles. Examples are the 1_{10}–1_{01} and 2_{12}–1_{01} lines in Figs. 3 and 4. Both the depth and the width of the absorption vary, as do the line wing strengths:
  (i) Absorption depth: if dust is optically thick (e.g., at 1669 GHz), the depth is independent of both X_0 and X_d as long as $\tau \gg 1$, and only depends on the radius where the dust turns optically thick, setting the continuum level. In Figs. 3 and 4 (*middle*) the 1669 GHz continuum-subtracted line is always at –0.2 K. If dust is optically thin (e.g., the 557 GHz 1_{10}–1_{01} line), the depth v of the absorption depends on both X_d and X_0 and is caused by self-absorption of the water in the cold outer region against the warm emission. Indeed, it is found that water at around 70–90 K acts as a warm background emitter and water at 20 K as the cold absorber.
  (ii) Absorption width: again there is a difference between high and low optical depths of dust. For 1669 GHz the width of the absorption depends on X_d, but not on X_0. For 557 GHz, there is no dependence on abundance. The width of the absorption is the same for varying X_0 (the temperature at which the water emits changes little), and even though the profiles appear different for different X_d, this can be attributed to the changing absorption depth, not width.
  (iii) Line wing strength: the strength of the line wing, which often contains the bulk of the line emission, is determined by the optical depth of the dust and gas. Most often, the peaks seen in the wings of the ground-state lines are still optically thick. The wings trace both X_d (see 1_{10}–1_{01} and 2_{12}–1_{01} lines in Fig. 3, left, middle), which still contain large columns of the gas, and X_0 (1_{10}–1_{01} and 2_{12}–1_{01} Fig. 4, left, middle), although in that case the relation is not straightforward. Line

pumping from the warm gas further inwards is the main origin of the dependency from $X_0 = 10^{-4}$ to 10^{-5}. However, if X_d and X_0 are low enough, the line wings turn optically thin and are significantly enhanced (Fig. 3) because higher temperatures are probed. This behavior is seen for a X_d/X_0 combination of $10^{-7}/10^{-6}$ where the line wings are brighter than for X_d/X_0 combinations of $10^{-7}/10^{-4}$ and $10^{-7}/10^{-5}$.

3.5. HIFI diagnostic lines

Although the beams for HIFI and the accompanying dilution factors are large compared to the physical size of the warm gas (see Table 3), the inner warm region is detectable through the higher excited states. The outer cold envelope is completely transparent for these lines. Considering the expected sensitivities of HIFI, a combination of different lines can constrain the water abundance profile. The $H_2^{18}O$ 2_{02}–1_{11} 994 GHz line in HIFI Band 4 is mostly optically thin and traces X_0, except at $H_2^{16}O$ X_d abundances higher than 5×10^{-6}. However, the line is weak (a few tens of mK) and needs at least a few hours of integration to be detected. A possible alternative is the high excitation $H_2^{16}O$ 3_{12}–3_{03} line in HIFI Band 4, which can be detected in roughly an hour of integration. It traces X_0 at high X_0 abundances, but for X_0 lower than 10^{-5}, emission coming from the colder outer part dominates, thus tracing X_d. This emission originates in the region with temperatures ranging from 70–100 K. Once the inner abundance X_0 is well-constrained, ground-state lines can in turn be used to constrain the abundance in the outer region. The bright wings of the 557 GHz line (HIFI Band 1) are detectable within a few minutes, but the entire line profile is needed for proper analysis (see Sect. 3.4). The dependence on X_d can be traced most accurately using the line profiles of the 1_{11}–0_{00} 1113 GHz para-H_2O and 1101 GHz para-$H_2^{18}O$ lines in Band 4, but resolving these profiles requires much longer integration times than the 557 GHz line. The 1667 GHz 2_{12}–1_{01} ortho-H_2O line in Band 6 is intrinsically brighter, but will take almost an hour of integration due to the low sensitivity of HIFI at this frequency. In addition, dust can become optically thick at this high frequency so that the line profile only traces the structure in the outer envelope.

The optically thick $H_2^{16}O$ 2_{02}–1_{11} 988 GHz line, with its optically thin $H_2^{18}O$ counterpart are the best candidates for determining the optical depth of water, but the $H_2^{18}O$ lines require significant integration time (see above). An alternative is provided by comparison between of the 548 GHz $H_2^{18}O$ and 557 GHz $H_2^{16}O$ ground-state lines, but $H_2^{18}O$ is still optically thick so that detailed modeling is required. The 1_{11}–0_{00} 1113 GHz, 2_{02}–1_{11} 988 GHz, and 2_{11}–2_{02} 752 GHz para-H_2O lines are well-suited to probing the physical structure of the envelope. Due to their different excitation energies and optical depths, these lines probe different environments within the protostellar envelope, and their line ratios are not affect by the uncertain ortho/para ratio.

3.6. Comparison with ISO-LWS data

The source L 483 was observed with ISO-LWS (Giannini et al. 2001). The para 2_{20}–1_{11} line at 2968 GHz (101 μm) was detected with a flux of $8.6 \pm 1.0 \times 10^{-20}$ W cm^{-2} and the ortho 2_{12}–1_{01} line at 1670 GHz (179.5 μm) was found to have an upper limit of 4.3×10^{-20} W cm^{-2}. The low LWS resolving power of $\lambda/\Delta\lambda = 200$ ($\sim$1500 km s^{-1}) was insufficient for determining the effect of any self-absorption or disentangling outflow components from quiescent envelope material. The best-fitting LVG model for the high-J CO lines gave a component of gas with $T = 850$–1800 K; it is expected that this hot gas contributes significantly to the water emission (Giannini et al. 2001).

The above models, corrected for the ISO beam of 80″, are compared to the observed intensity. Our models show a strong absorption into the dust for both lines with optically thin line wings. Integrated intensities range from -7×10^{-22} up to 17×10^{-20} W cm^{-2} for the 2_{20}–1_{11} line and from 0.9×10^{-20} W cm^{-2} to 16×10^{-20} W cm^{-2} for the ortho 2_{12}–1_{01} line for different X_0–X_d combinations. The best fit, using both the detection and upper limit, is found for an outer abundance of 10^{-7} and an inner abundance between 10^{-6} and 10^{-5}. The detected line is reproduced within 30%, while the upper limit is only 50% higher than the intensity produced by the model. For lower values of X_d, around 10^{-8}, the integrated emission in our model is almost an order of magnitude lower than the observed 2_{20}–1_{11} line. Such low outer abundances are found for cold regions in the envelopes around high-mass YSOs (Boonman et al. 2003), but appear inconsistent with the data for this low-mass YSO, unless the detected emission originates fully in the outflow. Higher inner abundances cannot be ruled out. However, the self-absorption in the models becomes stronger, resulting in a worse fit to the detected line and upper limit.

Other water lines within the ISO-LWS domain were not detected. The derived upper limits were found to be at least a factor 5 higher than fluxes predicted from all possible models. At short (>80 μm) wavelengths, the difference is a few orders of magnitude. Since all lines are unresolved, no conclusion can be reached as to whether the detected water emission is dominated by outflow contributions or by thermal excitation within the circumstellar envelope with a high abundance. This example illustrates the need for spectrally and spatially resolved data of a number of lines to disentangle the different physical components.

4. General parameter study

Table 6 and Figs. 5 and 6 present the results for a grid probing the parameters from Table 1 for a constant abundance combination of 10^{-4} for X_0 and 10^{-7} for X_d. Results for the full grid, including all probed abundances, can be found in the online appendix. The main variables of the grid – the luminosity, the density, and the density profile steepness – are discussed within this section. The dependence on abundance mirrors the behavior seen for the L 483 model discussed in Sect. 3. For most combinations of envelope parameters, the $H_2^{16}O$ transitions studied here are optically thick, sometimes with optically thin line wings. For $H_2^{18}O$ lines, most transitions are optically thin, although the three ground state lines are optically thick at line center. The only optically thin $H_2^{16}O$ lines are those for which the upper level of the transition has an excitation temperature above 200–250 K, specifically the lines with $J = 3$ and higher. These lines are only optically thin if the densities are low enough, $<10^7$ cm^{-3}, and abundances are low, $X_0 < 10^{-5}$ and $X_d < 10^{-7}$. For typical low-mass envelopes, such densities are only encountered within the inner region, where enhanced abundances are found. Thus, because many higher excited $H_2^{16}O$ lines become optically thick only in the very dense warm inner region, they are still good tracers of the inner region (see Sect. 3.3.1 and Fig. 4 right). For high densities and thus higher envelope masses, the larger dust column plays a major role by heavily influencing the water line emission. This is discussed in Sect. 5.

Table 6. Integrated intensities, $\int T_{\rm MB}\Delta V$ [K km s^{-1}], for H_2O lines in the wide parameter grid for an abundance combination of $X_0 = 10^{-4}$ and $X_{\rm d} = 10^{-7}$.

Transition	Integrated intensity ($\int T_{\rm MB}\Delta V$ [K km s^{-1}])					
	Lum. (w. $n_0 = 10^6$ cm^{-3})			Dens. (w. $L = 7\ L_\odot$)		
	2	7	25	0.4	1	5
			$p = 1.5$			
			Ortho-H_2O transitions			
1_{10}–1_{01}	0.37	0.95	0.70	0.43	0.95	2.1
2_{12}–1_{01}	0.35	0.36	–1.2	0.30	0.36	–4.4
2_{21}–2_{12}	0.29	0.87	1.5	0.60	0.87	0.74
3_{12}–3_{03}	0.21	0.60	1.5	0.38	0.60	0.89
3_{12}–2_{21}	0.21	0.67	1.6	0.40	0.67	0.84
3_{21}–3_{12}	0.37	1.1	2.7	0.59	1.1	1.7
			Para-H_2O transitions			
1_{11}–0_{00}	0.13	1.0	0.31	0.43	1.0	1.6
2_{02}–1_{11}	0.58	1.5	3.0	0.72	1.5	1.1
2_{11}–2_{02}	0.34	1.0	2.0	0.41	1.0	2.7
2_{20}–2_{11}	0.31	1.0	2.3	0.47	1.0	1.4
3_{31}–4_{04}	4.3(–2)	0.15	0.58	0.18	0.15	1.3(–3)
4_{22}–3_{31}	4.1(–2)	0.13	0.48	0.13	0.13	9.6(–2)
4_{22}–4_{13}	9.5(–2)	0.26	0.74	0.18	0.26	2.3(–3)
5_{24}–4_{31}	5.0(–2)	0.15	0.57	0.16	0.15	8.7(–2)
			$p = 2.0$			
			Ortho-H_2O transitions			
1_{10}–1_{01}	0.12	0.24	0.19	0.10	0.24	0.82
2_{12}–1_{01}	0.89	-1.6	–3.1	0.71	–1.6	–5.0
2_{21}–2_{12}	0.13	0.14	0.15	0.13	0.14	–1.4
3_{12}–3_{03}	0.12	0.47	1.3	0.35	0.47	0.51
3_{12}–2_{21}	0.13	0.48	1.2	0.29	0.48	0.49
3_{21}–3_{12}	0.20	0.87	2.1	0.45	0.87	1.2
			Para-H_2O transitions			
1_{11}–0_{00}	0.30	9.4(–2)	0.23	0.52	9.4(–2)	9.0(–2)
2_{02}–1_{11}	0.65	1.4	3.1	0.90	1.4	1.8
2_{11}–2_{02}	0.46	0.94	2.1	0.56	0.94	2.2
2_{20}–2_{11}	0.32	0.78	2.1	0.54	0.78	1.3
3_{31}–4_{04}	–3.7(–3)	–6.7(–3)	0.13	7.1(–2)	–6.7(–3)	–1.2(–3)
4_{22}–3_{31}	1.0(–2)	5.9(–2)	0.31	9.3(–2)	5.9(–2)	2.3(–3)
4_{22}–4_{13}	4.7(–2)	0.19	0.74	0.22	0.19	8.1(–2)
5_{24}–4_{31}	8.3(–3)	6.5(–2)	0.34	0.11	6.5(–2)	–6.9(–3)

Columns 2 to 4 show the luminosity variation with a density of 10^6 cm^{-3}. Columns 5 to 7 show the variation of density with a luminosity of 7 $L_\odot$.

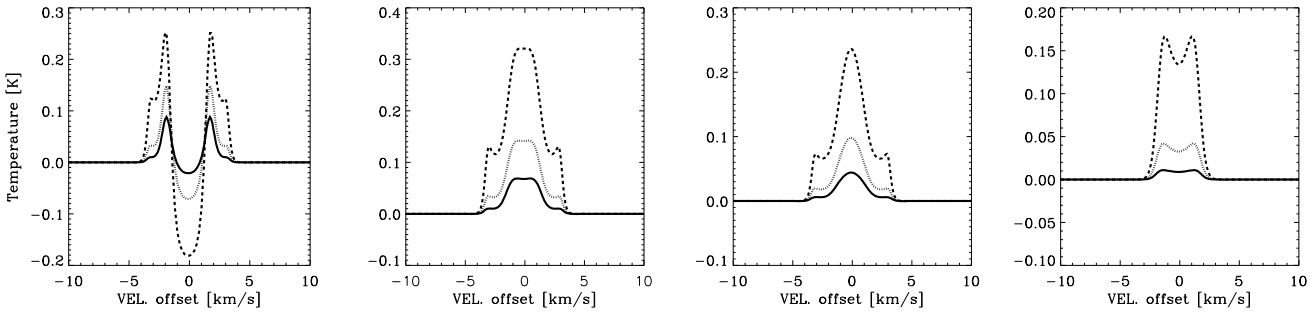

Fig. 5. Examples of the luminosity dependence of line profiles for a model with $p = 1.5$, $X_0 = 10^{-4}$, $X_{\rm d} = 10^{-8}$, $n_0(H_2) = 10^6$ cm^{-3}. *From left to right* are shown the 1_{11}–0_{00} 1113 GHz, 2_{02}–1_{11} 988 GHz, 2_{11}–2_{02} 752 GHz, and 3_{31}–4_{04} 1893 GHz lines. Luminosities are 2 (solid), 7 (dot), and 25 (dash) $L_\odot$. These lines reflect the different characteristic line profiles discussed in Sect. 3.4. It can be seen that the line shapes stay the same with increasing luminosity, while the line strengths and depths of the absorption are stronger at higher luminosities.

4.1. Luminosity

Figure 5 shows four lines for various luminosities. For all lines, both the line strength and the absorption features are stronger for higher luminosities. For optically thin lines, a best fit can be found with a slope that has a power-law index of ~0.8, i.e. $I \propto L^{0.8}$. Figure 7 shows two such power laws for the 2_{20}–2_{11} 1228 GHz line that differentiate between the exact conditions and correspond to 0.45 $L^{0.8}$ and 0.15 $L^{0.8}$. The slope of the power law is determined by the temperature profile, which determines the amount of warm gas present in the dense inner region, and the filling factor of this warm gas within the beam. This filling

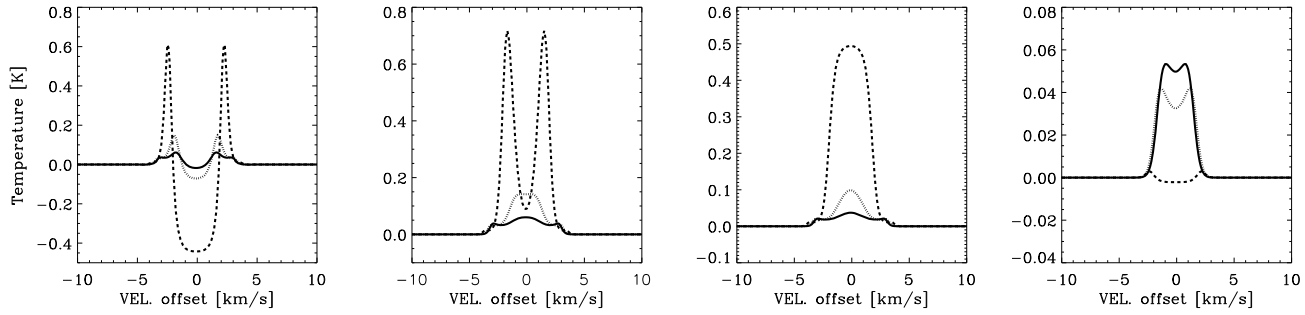

Fig. 6. Examples of the density dependence of line profiles for a model with $p = 1.5$, $X_0 = 10^{-4}$, $X_d = 10^{-8}$, $L = 7\ L_\odot$. *From left to right* are shown the 1_{11}–0_{00} 1113 GHz, 2_{02}–1_{11} 988 GHz, 2_{11}–2_{02} 752 GHz, and 3_{31}–4_{04} 1893 GHz lines. Densities are 4×10^5 (solid), 10^6 (dot), and 5×10^6 (dash) cm^{-3}. For most lines, the higher density, and thus higher water column, increases the emission, although absorption features are also enhanced. For the 3_{31}–4_{04} line at 1893 GHz, the dust becomes optically thick at lower temperatures (i.e. larger radii) within the envelope for higher densities.

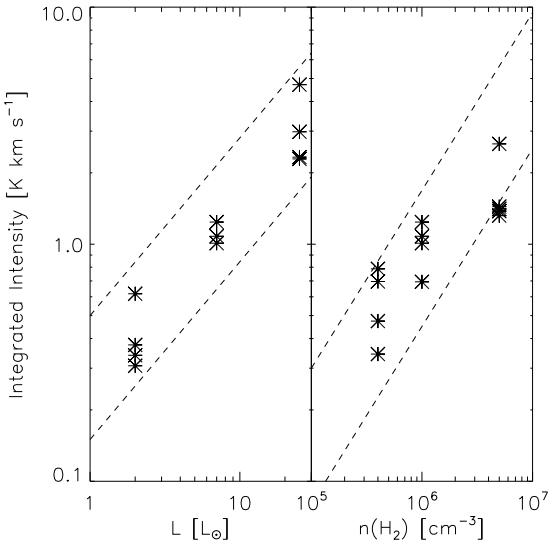

Fig. 7. The modeled integrated intensity of the optically thin 2_{20}–2_{11} 1228 GHz line for $X_0 = 10^{-4}$. Intensities are shown for the 3 different values of X_d for a constant density of 10^6 cm^{-3} (*left*) and for a constant luminosity of 7 $L_\odot$ (*right*). Power laws with indices of 0.8 (*left*) and 0.75 (*right*) are over-plotted. In the *right panel*, at 5×10^6 cm^{-3}, this line becomes optically thick for $X_d = 10^{-6}$, with its intensity dropping below the relation.

factor is not readily apparent, since models have different values for R_{in} and different radii where $T = 100$ K is reached depending on luminosity and density profile (see Table 2). The peak temperatures of these optically thin lines naturally follow a similar dependence. Even for lines that display an optically thick line center (e.g., the 3_{31}–4_{04} line in Fig. 5), the peak temperatures depend on luminosity in a similar way to the completely optically thin lines.

For optically thick lines, a more complex dependency is seen in Fig. 5 (e.g., the 1_{11}–0_{00} line). For such self-absorbed lines, the wings (which are optically thin) increase with L, while any absorption features also become more prominent. Although the peak temperatures do not follow the proposed power law of the optically thin lines, they will become easier to detect for more luminous sources.

4.2. Density

Figure 6 shows four lines for a range of densities, varying by more than an order of magnitude, corresponding to envelope masses ranging from 0.15 to 1.93 $M_\odot$. The density at 1000 AU has a strong influence on the water line emission. For optically thin lines, models with a constant p and constant luminosity show that a power law with an index of 0.75 accurately describes the dependence of line strengths on $n_0(H_2)$ (see Fig. 7). For optically thick lines, the line will decrease in strength at higher densities, since the emission from the warm inner part is veiled behind a larger, cold water column.

A higher density can also result in the dust becoming optically thick. This has an effect on the higher excited lines at high frequencies. For example, the optically thin 3_{31}–4_{04} 1893 GHz line (see Fig. 6, right) decreases by nearly two orders of magnitude in strength when the density increases from 0.4×10^6 to 5×10^6 cm^{-3}. The dust is optically thin in the low-density models and optically thick at high density. Since the emission of this higher excitation line originates in the warm inner region, optically thick dust can obscure over 99% of the emission of this high frequency line (see Sect. 5).

4.3. Density profile index

The steepness of the power law used to define the density distribution, p, also influences water line emission. Table 6 shows that lines differ subtly between $p = 2$ and $p = 1.5$. The line intensities of models with $p = 2$ are lower by a factor ranging from 0.5 to 3 than those for models with $p = 1.5$. Absorption features also differ in their depths for similar models with only p varied. This is caused by differing temperature profiles within the Herschel beams. Assuming equal $n_0(H_2)$ at 1000 AU, the warm ($T > 100$ K) region is significantly smaller for a model with $p = 2$ than for $p = 1.5$. Although local densities are higher by almost an order of magnitude, the beam dilution is too severe to overcome such small regions.

4.4. $H_2^{18}O$

The models were also calculated for the isotopologue $H_2^{18}O$. Similar to the L 483 models, transitions connected with the ground state lines are optically thick for all models. $H_2^{18}O$ excited lines with $J_{up} = 2$ and 3 do have optically thick centers for some combinations of abundance, luminosities and/or densities, but are optically thin at densities below 10^6 cm^{-3}. Higher

excitation $H_2^{18}O$ lines are always optically thin. The best-fit power law slopes for the optically thin $H_2^{18}O$ lines are the same as those for $H_2^{16}O$. Of course, these conclusions are limited by the optical depth of dust at the frequency of the line, since $H_2^{18}O$ lines at high frequencies are affected by dust. The precise frequency depends on the combination of luminosity and the density profile (Sect. 5). Results for $H_2^{18}O$ can be found in the online appendix.

4.5. Line profiles

The H_2O line profiles shown in Figs. 5 and 6 all contain optically thin and optically thick parts as discussed in Sect. 3.4. Since the line wings of most transitions are optically thin, a "bump" is present in these wings at the velocity for which that particular line becomes optically thick. This velocity depends solely on the total column of water at this velocity and not on the luminosity. The height of this bump is determined by both the luminosity and the density profile. The line center changes according to the actual optical depth of both the dust and the water itself. Line centers can (i) be effectively thin and show a Gaussian profile, (ii) be dominated by a small region and be flat-topped, (iii) show a self-absorption feature determined by the optical depth of the line alone; (iv) have absorption into the dust continuum.

4.6. Model limitations

Our spherically symmetric envelope models have several limitations, which can affect the interpretation of observed line strengths.

- The presence of a large velocity gradient, such as seen in infall and rotation of envelopes around high-mass stars, can significantly broaden the water line and simultaneously make it less optically thick. The velocity field in these models was taken to be small, with an average infall velocity of 4 km s^{-1} at $R_{\rm in}$. For low-mass sources, such an infall velocity combined with a turbulent width of 1 km s^{-1} has been shown to accurately reproduce observed emission line profiles (Jørgensen 2004).
- Outflow contributions. No outflow contribution has been taken into account in our models. It is assumed that emission from outflow material can be identified with sufficient spectral resolution in observational data with Herschel-HIFI. However, material heated by outflow shocks in high-density regions will not necessarily be accelerated to high velocities. This material can add significantly to the emission of water lines, but requires a detailed shock model to quantify it (e.g., Kaufman & Neufeld 1996). In addition, outflow cavities allow emission from the high-density regions of the inner envelope to escape along paths with much lower density than encountered in the cold outer envelope.
- Large extended molecular cloud or fore-ground cloud contributions can both emit rotational water lines or absorb radiation coming from the protostellar envelope. This is especially likely for the three transitions connected to the ground-states of ortho- and para-water. For example, for a cloud column density of 10^{22} cm^{-2} and an assumed water abundance of 10^{-8} with a gas density of 10^5 cm^{-3}, the ground state ortho-H_2O 557 GHz line will have an intensity of 50 mK if the emission fills the beam. The optical depth of this line is large enough, $\tau \approx 20$, to absorb radiation coming from behind this cloud. Results from SWAS and ODIN (See Sect. 6.2) indeed do not show the deep absorption in the 557 GHz line, seen in Figs. 3–6. It is likely that extended cold cloud material dominates close (<0.5 km s^{-1}) to the line center in these data due to the much larger observing beams than Herschel. For excited lines, emission and optical depth in a foreground cloud are negligible. At high (>1 THz) frequencies, the dust within such cloud complexes can, however, absorb the emission from excited water.
- A large massive gas disk can contribute to the emission of water. However, most gas within disks is at low ($T \sim 30$ K) temperatures. Most of the water will be frozen out, except in the inner few AU and in the warm surface layers. In addition, high dust columns can completely obscure frequencies above 1 THz. Water emission from disks is thus expected to be orders of magnitude lower for lines at all frequencies, except for the transitions connected to the ground state below 1 THz. However, the small angular size of disks causes much of the emission to be diluted to much lower values (a few mK) within the Herschel beam than commonly found for envelopes (a few 100 mK to a few K).

Table 7. Integrated intensity and peak brightness of lines with and without dust for a model with $p = 1.5$, $L = 7\ L_{\rm bol}$ and $n_{\rm H_2} = 1 \times 10^6$ cm^{-3}.

Transition	Dust		No dust	
	Intensity [K km s^{-1}]	$T_{\rm peak}$ [K]	Intensity [K km s^{-1}]	$T_{\rm peak}$ [K]
1_{10}–1_{01}	0.95	0.47	1.41	0.65
2_{12}–1_{01}	–2.6(–2)	0.26	0.16	0.39
3_{12}–3_{03}	0.67	0.18	0.39	0.06

5. Effects on H_2O excitation and line formation: dust and micro-turbulence

5.1. Dust

The presence of dust in protostellar envelopes influences water emission lines significantly in two ways, as can be seen in Table 7. First, the dust can become optically thick, preventing water emission from deep in the envelope to escape. Second, the far-infrared radiation can pump the water lines. Dust becomes optically thick at specific columns, depending on the value of the opacity, κ, at a given frequency (see Fig. 5c in Ossenkopf & Henning 1994, for the precise relation). Since $\kappa_\nu \propto \nu^\beta$, with the dust opacity index β typically 1.5, this is especially likely at higher frequencies. Column 4 of Table 8 shows the total gas and dust column densities needed to reach a dust optical depth equal to 1 for each line.

Figure 8 illustrates this effect in a cartoon for two different envelope models. Two models, one with low density (low $M_{\rm env} \approx 0.15\ M_\odot$) and one with high density (high $M_{\rm env} \approx 1.93\ M_\odot$), are compared for two ground-state lines. The dust at 557 GHz only becomes optically thick for the more massive envelope due to very high column densities, while the low-density model remains optically thin throughout. The $\tau = 1$ surfaces correspond to temperatures well over 100 K. Since the 557 GHz water line is optically thick at lower columns, the dust will have no effect on this line, except for weakening the line due to dust absorption. Even the $H_2^{18}O$ column is large enough to prevent the dust opacity from influencing the 548 GHz line. In contrast, the dust at 1669 GHz becomes optically thick at a much smaller column, which corresponds to a radius and temperature much farther out into the envelope. The actual radius depends on the

Table 8. The dust properties at selected water line frequencies for four typical models. The column density N_{H_2} required to produce $\tau = 1$ for the dust at each frequency is given with the corresponding radii and temperatures.

Transition	Frequency	κ_{OH5}	N_{H_2}	r and T ($\tau_{dust} = 1$)							
				Model 1[c]		Model 2[d]		Model 3[e]		Model 4[f]	
	GHz	10^{-2} cm^{2}g^{-1}[a]	10^{23} cm^{-2}	AU	K	AU	K	AU	K	AU	K
Ortho-H_2O transitions											
1_{10}–1_{01}	556	4.56	54.8	–[b]	–	–	–	–	–	–	–
2_{12}–1_{01}	1669	32.7	7.6	45	97	62	73	9	188	–	–
2_{21}–2_{12}	1661	32.3	7.2	48	92	63	72	10	179	–	–
3_{12}–3_{03}	1097	17.3	14.5	–	–	32	111	–	–	–	-
3_{12}–2_{12}	1153	18.5	13.5	15	240	34	107	–	–	–	–
3_{21}–3_{12}	1162	18.7	13.3	16	217	35	105	–	–	–	–
Para-H_2O transitions											
1_{11}–0_{00}	1113	17.7	14.1	–	–	33	109	–	–	–	–
2_{02}–1_{11}	987	14.4	17.3	–	–	27	128	–	–	–	–
2_{11}–2_{02}	752	8.45	29.5	–	–	16	213	–	–	–	–
2_{20}–2_{11}	1228	20.0	12.4	18	185	37	101	–	–	–	–
3_{31}–4_{04}	1893	40.9	6.1	64	78	74	65	12	154	–	–
4_{22}–3_{31}	916	12.2	20.4	–	–	38	99	–	–	–	–
4_{22}–4_{13}	1207	19.6	12.7	17	193	23	144	–	–	–	–
5_{24}–4_{31}	970	13.9	17.9	–	–	26	131	–	–	–	–

[a] Total gas and dust; [b] – indicates that the dust is optically thin throughout the entire envelope; [c] see text, $L = 7\ L_\odot$, $p = 1.5$, $n_0 = 5 \times 10^6$ cm^{-3}; [d] see text, $L = 7\ L_\odot$, $p = 2$, $n_0 = 5 \times 10^6$ cm^{-3}; [e] see text, $L = 2\ L_\odot$, $p = 2$, $n_0 = 4 \times 10^5$ cm^{-3}; [f] see text, $L = 25\ L_\odot$, $p = 1.5$, $n_0 = 1 \times 10^6$ cm^{-3}.

model in question. In the low-density model, the dust only turns optically thick at radii close to the 100 K water evaporation radius, while dust in the high-density model already obscures the line in the outer regions of the envelope. Optically thin lines at this frequency will not be able to probe the warm inner region, since the optically thick dust effectively absorbs all water line emission.

Figure 9 shows example spectra of the 1_{10}–1_{01} line at 557 GHz, 2_{12}–1_{01} line at 1669 GHz and the $3_{12} - 3_{03}$ line at 1097 GHz for a model with $L = 7\ L_\odot$, $n_{H_2} = 1 \times 10^6$ cm^{-3}, $p = 1.5$, $X_0 = 10^{-4}$, and $X_d = 10^{-7}$, with and without dust. The spectra with dust are significantly weaker by up to 50%, even for optically thin dust at 557 GHz, since dust within the line of sight absorbs the water line photons. Lines that are optically thin at a frequency where optically thick dust exists are weaker by factors up to a few or more if dust is present, due to less water being "visible". Optically thin lines can be pumped by far-infrared dust radiation coming from the region at radii larger than the $\tau = 1$ surface of the dust at the frequency of the line.

For each envelope model, the column density of dust depends on a combination of luminosity L (through the location of R_{in}, Table 2) and envelope structure parameters n_0 and p. If the $\tau = 1$ surface is approximated as a hard surface where all water photons are absorbed, a typical temperature can be extracted for each combination of L, n_0, and p. This temperature is the upper limit to which water lines can probe for each model before dust becomes optically thick. Table 8 presents the $\tau = 1$ temperatures for four astronomically distinct models, based on the results from Table 6 of Jørgensen et al. (2002). Model 1, with $L = 7\ L_\odot$, $p = 1.5$, and $n_0 = 5 \times 10^6$ cm^{-3}, corresponds to a very young Class 0 YSO, which is dominated by a large, cold, and massive protostellar envelope. A good example is the well-studied NGC 1333 IRAS 4B source in the Perseus molecular cloud. Lines with a frequency above 1600 GHz are unable to probe the region with $T > 100$ K. Dust is optically thin throughout the envelope for frequencies lower than a 1000 GHz. Model 2, with $L = 7\ L_\odot$, $p = 2$ and $n_0 = 5 \times 10^6$ cm^{-3}, has similar parameters but its mass is more centrally condensed. Due to the very high column densities, dust becomes optically thick at all frequencies above 700 GHz, making it even more difficult to probe the central warm region than in Model 1. Highly excited water lines are effectively shielded from observers within this envelope at all frequencies. The third model, $L = 2\ L_\odot$, $p = 2$, $n_0 = 4 \times 10^5$ cm^{-3}, corresponds to a more evolved source with a low luminosity and a small envelope with most of the mass concentrated in the center due to a steep density profile. The relative amount of warm gas in this envelope is significantly higher. Such a model would correspond to most Class I sources, e.g., TMC-1A. The last model included has $L = 25\ L_\odot$, $p = 1.5$, and $n_0 = 1 \times 10^6$ cm^{-3} which corresponds to a higher luminosity source, but with a low total mass. The mass of the envelope is distributed over larger radii and the luminosity is higher. For these last two models, dust will not hide the inner parts of the envelope at all. Only the very warm region ($T > 150$ K) is veiled near the inner radius of Model 3.

5.2. Micro-turbulence

The structure of micro-turbulence, defined in our models as a velocity dispersion, during the embedded phases of star formation is not well known, and theoretical models do not yet agree on a correct treatment. A good review of the theoretical considerations and problems is given in Ward-Thompson & Buckley (2001, their Sect. 3.2). Jørgensen (2004) concludes that the inclusion of micro-turbulence as a velocity dispersion gives a more accurate reproduction of line intensities and profiles as opposed to the inclusion of infall (Jørgensen et al. 2005). Ward-Thompson & Buckley (2001, Sect. 4.6) test different values of micro-turbulence, as well as different power-law values for the variation of micro-turbulence with radius. This results in a large variation in the molecular line profiles of CS and HCO^+. Similarly, Fig. 10 shows that the choice of the velocity dispersion can have a strong effect on all water lines, both optically thick and thin. All three lines (557, 1669, and 1097 GHz) show large differences in both line profile and in total integrated emission up to a factor of 3, when the velocity dispersion is varied between 0.83 ($b = 0.5$), 1.67 ($b = 1$) and 3.34 ($b = 2$) km s^{-1}. Absorption both into the continuum and in the line are broader

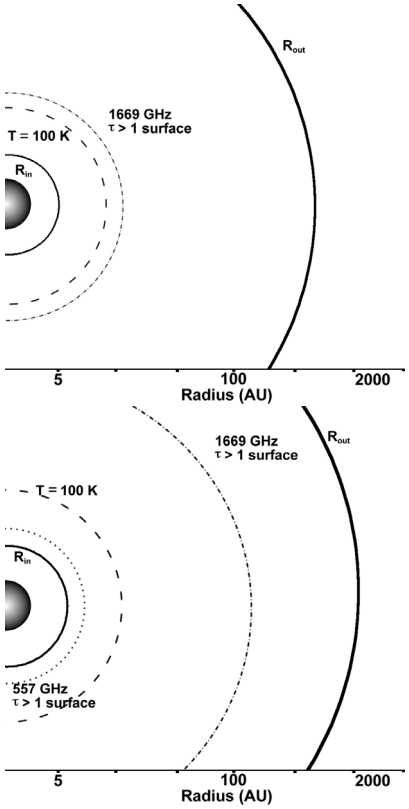

Fig. 8. Cartoon of protostellar envelope models. For two different models, the $\tau = 1$ surfaces at 557 and 1669 GHz for the dust are shown. A model with low-density ($n_0(H_2) = 4 \times 10^5$ cm^{-3}, $M = 0.15\ M_\odot$) is shown in the *top panel*; here the 557 GHz line contour is absent, since dust is optically thin throughout the envelope at this frequency. A model with a high density ($n_0(H_2) = 5 \times 10^6$ cm^{-3}, $M = 1.93\ M_\odot$) is shown in the bottom panel. The long-dashed line indicates the $T = 100$ K contour. In both models, the 1669 GHz line is unable to probe the inner warm region, regardless of its own optical depth, since the dust $\tau = 1$ surface lies far outside the $T = 100$ K radius.

for higher values of micro-turbulence, while peak separation increases with increased velocity dispersion. Optically thin lines and line wings broaden if b is larger. Such effects are similar to those found by Ward-Thompson & Buckley (2001).

For molecular lines in low-mass protostellar envelopes, Ward-Thompson & Buckley (2001) and Jørgensen et al. (2005) both adopt a constant value for the micro-turbulence with radius. In our case, a velocity dispersion, $\Delta V \sim 1.67$ km s^{-1} ($b = 1$ km s^{-1}), has been chosen to best reproduce line emission for a wide variety of molecules in sources such as L483, including CO, CS, but also complex molecules such as H_2CO and CH_3OH, tracing both the warm and cold regions. We recommend that for the modeling of water lines from specific sources, the velocity dispersion for the cloud in question be adopted as derived from other molecular lines.

6. Observational studies

The conclusions presented in previous paragraphs can be compared to current observational studies. However, due to the approximations used within the models and the unique combinations of parameters for individual sources, it is recommended that these models be used only as a starting point for interpreting water emission of protostellar envelopes from specific sources. As discussed in Sect. 4.6, there are several factors that will complicate any analysis of observed water lines. To compare the envelope models presented above with any individual observation other than those from Herschel, the line intensities have to be corrected for the actual beam size of the telescope.

6.1. ISO-LWS

Water has been detected in several low-mass YSOs (both Class 0 and Class I) with ISO-LWS such as NGC 1333 IRAS 2/4, IRAS 16293-2422, Elias 29, L 1448, L 483, and SSV 13 (e.g., Liseau et al. 1996; Ceccarelli et al. 1999; Nisini et al. 1999; Giannini et al. 2001; Maret et al. 2002). Up to 14 water lines were detected, ranging from 180.5 μm to 67.3 μm. In most sources the total number of lines is significantly lower, but sufficient for proving the existence of water. For example, only a single line was detected for the Class I source Elias 29 (Ceccarelli et al. 1999).

As an illustration, we consider the case of NGC 1333 IRAS4A/B, for which Maret et al. (2002) report the emission of 14 water lines, together with high-J CO, OH, [O I], and [C II]. A model was put forward to explain the origin of these FIR lines using a collapsing envelope model without an outflow. Based on the model developed by Ceccarelli et al. (1996), the envelope and stellar parameters were derived from the best fit model to the 14 water lines. The water abundances in the envelope were found to include a jump at 100 K with a best fit of $X_0 = 5 \times 10^{-6}$ and $X_d = 5 \times 10^{-7}$. A lower inner abundance is excluded by their model results, but a higher X_0 abundance of the order of 5×10^{-5} cannot be excluded.

The physical parameters derived by Jørgensen et al. (2002) and abundances proposed by Maret et al. (2002) correspond best with our model to $n_0 = 10^6$ cm^{-3}, $L = 7\ L_\odot$, and $p = 1.5$ with abundances 10^{-6} for X_0 and $10^{-6}/10^{-7}$ for X_d . However, our predicted line strengths differ from the observed and predicted line strengths in Maret et al. (2002), especially for low excitation lines. Our 2_{21}–2_{12} and 2_{12}–1_{01} predictions are 0.5 10^{-20} and 1.1×10^{-20} W cm^{-2} for the $10^{-6}/10^{-7}$ abundance combination within the ISO-LWS beam, significantly lower than the observed values of 11 and 27×10^{-20} W cm^{-2}. Although an inner abundance of 10^{-4} produces brighter lines for the presented models, these lines are still an order of magnitude lower than the observed fluxes in Maret et al. (2002). The most likely explanation is the different treatment of dust between the two models, which lowers the fluxes of the high-frequency lines in our case. However, this also suggests that our models can only explain the ISO-LWS fluxes if there are cavities in the envelopes through which the photons can escape. Recent results with the Spitzer Space Telescope show numerous spectrally unresolved water lines from 20 to 30 μm, which suggest that NGC 1333 IRAS 4B is indeed viewed almost face-on, allowing the ro-vibrational lines to escape the protostellar system unhindered along the outflow axis (Watson et al. 2007). This can also help the longer wavelength lines coming from the inner envelope. Another possibility is that significant contributions come from large-scale outflows. This is confirmed by SWAS (see Sect. 6.2).

6.2. SWAS

SWAS[5] observed only the ground-state transition of o-H_2O at 557 GHz and o-$H_2^{18}O$ at 548 GHz. Although the beam of SWAS ($3.3' \times 4.5'$) is significantly larger than for ISO-LWS, the

[5] See http://cfa-www.harvard.edu/swas/ for more information.

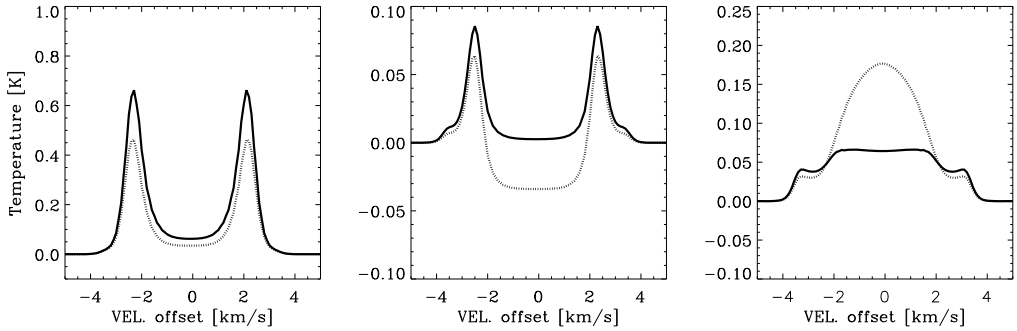

Fig. 9. Example spectra of the 1_{10}–1_{01} 557 GHz line (*left*), 2_{12}–1_{01} 1669 GHz line (*middle*) and 3_{12}–3_{03} 1097 GHz line (*right*) for a model with $p = 1.5$, $L = 7\ L_{\odot}$ and $n_{\rm H_2} = 1 \times 10^6$ cm^{-3}. The solid lines represent the spectra with no dust within the envelope, while the dotted line shows the same line with dust included in the model. The influence of dust can be clearly seen. The peaks of the optically thick lines are reduced in strength, the depth of the absorption changes, and the optically thin lines are significantly pumped by far-infrared radiation.

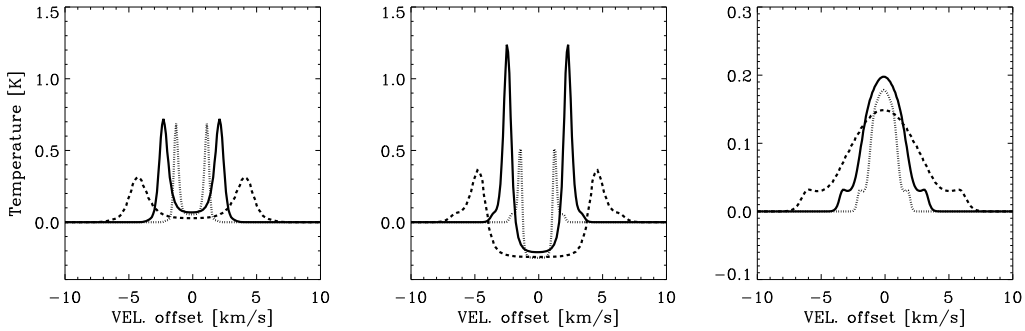

Fig. 10. Example spectra of the 1_{10}–1_{01} 557 GHz line (*left*), 2_{12}–1_{01} 1669 GHz line (*middle*), and 3_{12}–3_{03} 1097 GHz line (*right*) for a model with $p = 1.5$, $L = 7\ L_{\odot}$, and $n_{\rm H_2} = 1 \times 10^6$ cm^{-3}. The dotted line is for a model with $\Delta V = 0.83$ km s^{-1}. The solid line for $\Delta V = 1.67$ km s^{-1}, and the dashed line for $\Delta V = 3.34$ km s^{-1}. The large effect of micro-turbulence for all lines can be seen clearly.

increased spectral resolution of better than 1 km s^{-1} spectrally resolves most lines in starforming regions.

SWAS observed the NGC 1333 IRAS4 region (Neufeld et al. 2000; Bergin et al. 2003) where, contrary to the analysis of Maret et al. (2002), they observed a wide (24.4 km s^{-1}) and bright ($\int T_A^* {\rm d}V = 0.5$–$1.9$ K km s^{-1}) line. It was concluded that these lines originate within the outflow of one or more sources inside the NGC 1333 region. The model proposed by Maret et al. (2002) would have produced a narrow (<4 km s^{-1}) and weak (0.02–0.04 K km s^{-1}) 557 GHz line for each source contained within the beam. Our grid gives a typical integrated intensity within a SWAS beam of $\int T_{\rm MB} {\rm d}V = 0.5$ K km s^{-1} for a $X_0/X_{\rm d}$ combination of $10^{-4}/10^{-6}$ with a typical line width of 6 km s^{-1}.

Ashby et al. (2000) report on SWAS data for B335, an isolated Class 0 source with a 3σ upper limit of <0.06 K km s^{-1}. Evans et al. (2005) used a wide variety of molecular emission lines to model the chemistry and physical structure of this source. The low luminosity (4.5 $L_{\odot}$) and low density (4×10^5 cm^{-3}) found by Evans et al. (2005) indicate that this class 0 source would be represented best by a model with $p = 1.5$, $L = 2\ L_{\odot}$ and $n_0({\rm H_2}) = 4 \times 10^5$ cm^{-3}. Our predicted 557 GHz line strength corrected for the much larger SWAS beam is 0.02–0.06 K km s^{-1} for outer abundances from 10^{-8} to 10^{-6}, just below the upper limits from SWAS. The only model that would have been detectable with SWAS has a constant abundance of 10^{-6}. The high jump abundance model with $X_0 = 10^{-4}$ and $X_{\rm d} = 10^{-6}$ cannot be ruled out, since most of the line is self-absorbed. A similar conclusion holds for most other Class 0 sources detected with SWAS.

Using the SWAS archive[6], upper limits were found on several Class I sources, including RCrA IRS 5 and 7. Only upper limits of 20–50 mK in peak temperature could be derived. These observed limits are higher by up to an order of magnitude than the predictions presented in Sect. 4 for models that would fit the physical parameters of Class I sources. The cold envelope material is constrained to 10″–30″, a small region within the SWAS beam. Thus, our models are consistent with the scarce observational data on Class I sources.

In summary, both the ISO and SWAS data stress the need for Herschel Space Observatory data to properly constrain the origin of the observed H_2O emission and distinguish large-scale and outflow contributions from the emission originating in the quiescent gas of the protostellar envelope.

7. Summary and conclusions

This paper presents several models that examine the excitation of water and its oxygen-18 isotopologue in envelopes around low-mass protostars, with parameters covering the entire range of luminosity and envelope characteristics of observed Class 0 and I sources. A model for the Class 0 source L 483 was used to illustrate the dependence of rotational water lines on the water

[6] See http://lambda.gsfc.nasa.gov/product/swas/ for more information.

abundances in the inner ($T > 100$ K) region X_0 and outer ($T < 100$ K) region X_d. In turn, a broader grid of models was explored for the full range of parameters and likely abundances. The main conclusions follow.

- The strengths and line shapes of all rotational water lines are sensitive to the physical parameters of the envelope. Thus, an accurate physical model, including a well-constrained density profile, is a necessary pre-requisite to modeling the water emission and derive abundances.
- Ground-state lines from both $H_2^{16}O$ and $H_2^{18}O$ become optically thick at low water columns. Even though water abundances are expected to be very low in the outer envelope (10^{-8} with respect to H_2), the ground-state lines are still dominated by emission from the cold ($T < 30$ K) outer ($r > 1000$ AU) envelope. Ground-state line profiles are characterized by a double-peak feature with an absorption around narrow, optically thin emission line wings. The total integrated intensity cannot be used to trace the water abundance. Spectrally resolving the ground state lines is essential if these lines are to be used as probes for the water abundance.
- Higher excitation lines ($E_{up} > 150$ K) are usually dominated by emission coming from the warm inner region. At very high excitation ($E_{up} > 200$–250 K), the lines are optically thin. Although these lines are weak (<0.4 K km s^{-1}), they provide valuable information about the characteristics of the warm gas present in the inner regions of the protostellar envelopes. Power laws with an index of 0.8 and 0.75 were found to accurately represent the dependence of optically thin lines on luminosity and density.
- $H_2^{18}O$ is a reliable alternative tracer of the abundances in both the warm ($T > 100$ K) and cold ($T < 100$ K) regions of the envelope. However, such lines are much weaker with predicted peak temperatures of only a few tens of mK, requiring very long integration times.
- The presence of dust strongly influences the emission of most water lines. The optical depth of dust, which depends on the luminosity (due to varying R_{in} in our models) and density profile parameters, can prevent optically thin water lines from escaping the inner envelope, resulting in orders of magnitude reduction of the water fluxes. In addition, even optically thin dust absorbs up to 50% of the total line emission. Furthermore, the far-infrared continuum can pump optically thin water lines.
- The value of the micro-turbulent velocity dispersion and the structure of any systematic velocity field can significantly influence the line profiles and intensities of all water lines. The adoption of a micro-turbulent width that is constant with radius, as inferred from line profile fits of other molecules such as CS and HCO^+, is expected to produce the best-fitting H_2O line profiles, but the actual values need to be determined on a source-by-source basis.

To conclude, although water is a complex molecule to model, total intenstities and line profiles of rotational water transitions can be used to constrain essential information about the protostellar envelope. The increased sensitivity and resolution, both spectrally and spatially available with HIFI and PACS on Herschel compared with previous missions, will provide the technology to observe water lines covering a wide range of excitations for the water molecule. The increased spectral resolution will be essential for locating the origin of warm gaseous water and understanding the structure of low-mass protostellar envelopes. Abundances in both the cold outer region and the warm inner region are best probed by a combination of lines and must include detailed line profiles.

Acknowledgements. T.v.K. would like to thank Dieter Poelman, Floris van der Tak, and Antonio Crapsi for valuable discussion concerning YSO envelope modeling in general and the use of RATRAN. T.v.K. and astrochemistry at Leiden Observatory are supported by a Spinoza grant and by grant 614.041.004 from the Netherlands Organization for Scientific Research (NWO).

References

Adams, F. C., Lada, C. J., & Shu, F. H. 1987, ApJ, 312, 788
André, P., Ward-Thompson, D., & Barsony, M. 1993, ApJ, 406, 122
André, P., Ward-Thompson, D., & Barsony, M. 2000, Protostars and Planets IV, 59
Ashby, M. L. N., Bergin, E. A., Plume, R., et al. 2000, ApJ, 539, L119
Bergin, E. A., & Snell, R. L. 2002, ApJ, 581, L105
Bergin, E. A., & Melnick, G. J. 2005, in Astrochemistry: Recent Successes and Current Challenges, ed. D. C. Lis, G. A. Blake, & E. Herbst, IAU Symp., 231, 309
Bergin, E. A., Kaufman, M. J., Melnick, G. J., Snell, R. L., & Howe, J. E. 2003, ApJ, 582, 830
Boogert, A. C. A., Hogerheijde, M. R., Ceccarelli, C., et al. 2002, ApJ, 570, 708
Boonman, A. M. S., Doty, S. D., van Dishoeck, E. F., et al. 2003, A&A, 406, 937
Butner, H. M., Charnley, S. B., Ceccarelli, C., et al. 2007, ApJ, 659, L137
Ceccarelli, C., Hollenbach, D. J., & Tielens, A. G. G. M. 1996, ApJ, 471, 400
Ceccarelli, C., Caux, E., Loinard, L., et al. 1999, A&A, 342, L21
Ceccarelli, C., Castets, A., Caux, E., et al. 2000, A&A, 355, 1129
Ceccarelli, C., Baudry, A., Caux, E., et al. 2001, in The Promise of the Herschel Space Observatory, ed. G. L. Pilbratt, J. Cernicharo, A. M. Heras, T. Prusti, & R. Harris, ESA SP-460, 219
Cernicharo, J., & Crovisier, J. 2005, Space Sci. Rev., 119, 29
Cernicharo, J., Thum, C., Hein, H., et al. 1990, A&A, 231, L15
Cernicharo, J., Bachiller, R., & Gonzalez-Alfonso, E. 1996, A&A, 305, L5
Charnley, S. B., Tielens, A. G. G. M., & Millar, T. J. 1992, ApJ, 399, L71
Charnley, S. B., Rodgers, S. D., & Ehrenfreund, P. 2001, A&A, 378, 1024
de Graauw, T., & Helmich, F. P. 2001, in The Promise of the Herschel Space Observatory, ed. G. L. Pilbratt, J. Cernicharo, A. M. Heras, T. Prusti, & R. Harris, ESA SP-460, 45
Doty, S. D. 2000, ApJ, 535, 907
Doty, S. D., & Leung, C. M. 1994, ApJ, 424, 729
Doty, S. D., & Neufeld, D. A. 1997, ApJ, 489, 122
Dubernet, M.-L., & Grosjean, A. 2002, A&A, 390, 793
Dubernet, M.-L., Daniel, F., Grosjean, A., et al. 2006, A&A, 460, 323
Elitzur, M., Hollenbach, D. J., & McKee, C. F. 1989, ApJ, 346, 983
Evans, II, N. J., Lee, J.-E., Rawlings, J. M. C., & Choi, M. 2005, ApJ, 626, 919
Faure, A., Crimier, N., Ceccarelli, C., et al. 2007, A&A, 472, 1029
Felli, M., Brand, J., Cesaroni, R., et al. 2007, A&A, 476, 373
Fraser, H. J., Collings, M. P., McCoustra, M. R. S., & Williams, D. A. 2001, MNRAS, 327, 1165
Furuya, R. S., Kitamura, Y., Wootten, A., Claussen, M. J., & Kawabe, R. 2003, ApJS, 144, 71
Gensheimer, P. D., Mauersberger, R., & Wilson, T. L. 1996, A&A, 314, 281
Giannini, T., Nisini, B., & Lorenzetti, D. 2001, ApJ, 555, 40
Goldsmith, P. F., & Langer, W. D. 1978, ApJ, 222, 881
Green, S., Maluendes, S., & McLean, A. D. 1993, ApJS, 85, 181
Grosjean, A., Dubernet, M.-L., & Ceccarelli, C. 2003, A&A, 408, 1197
Harwit, M., Neufeld, D. A., Melnick, G. J., & Kaufman, M. J. 1998, ApJ, 497, L105
Helmich, F. P., van Dishoeck, E. F., Black, J. H., et al. 1996, A&A, 315, L173
Hogerheijde, M. R., & van der Tak, F. F. S. 2000, A&A, 362, 697
Ivezić, Z., & Elitzur, M. 1997, MNRAS, 287, 799
Jacq, T., Henkel, C., Walmsley, C. M., Jewell, P. R., & Baudry, A. 1988, A&A, 199, L5
Jacq, T., Walmsley, C. M., Henkel, C., et al. 1990, A&A, 228, 447
Jørgensen, J. K. 2004, A&A, 424, 589
Jørgensen, J. K., Schöier, F. L., & van Dishoeck, E. F. 2002, A&A, 389, 908
Jørgensen, J. K., Schöier, F. L., & van Dishoeck, E. F. 2004, A&A, 416, 603
Jørgensen, J. K., Schöier, F. L., & van Dishoeck, E. F. 2005, A&A, 437, 501
Jørgensen, J. K., Johnstone, D., van Dishoeck, E. F., & Doty, S. D. 2006, A&A, 449, 609
Jørgensen, J. K., Bourke, T. L., Myers, P. C., et al. 2007, ApJ, 659, 479
Kaufman, M. J., & Neufeld, D. A. 1996, ApJ, 456, 611
Lada, C. J. 1987, in Star Forming Regions, ed. M. Peimbert, J. Jugaku, & P. W. J. L. Brand (Dordrecht: Reidel), IAU Symp., 115, 1
Liseau, R., Ceccarelli, C., Larsson, B., et al. 1996, A&A, 315, L181

Maret, S., Ceccarelli, C., Caux, E., Tielens, A. G. G. M., & Castets, A. 2002, A&A, 395, 573
Maret, S., Ceccarelli, C., Caux, E., et al. 2004, A&A, 416, 577
Motte, F., & André, P. 2001, A&A, 365, 440
Myers, P. C., Evans, II, N. J., & Ohashi, N. 2000, Protostars and Planets IV, 217
Neufeld, D. A., & Kaufman, M. J. 1993, ApJ, 418, 263
Neufeld, D. A., Snell, R. L., Ashby, M. L. N., et al. 2000, ApJ, 539, L107
Nisini, B., Benedettini, M., Giannini, T., et al. 1999, A&A, 350, 529
Nisini, B., Giannini, T., & Lorenzetti, D. 2002, ApJ, 574, 246
Ossenkopf, V., & Henning, T. 1994, A&A, 291, 943
Parise, B., Caux, E., Castets, A., et al. 2005, A&A, 431, 547
Park, G., & Choi, M. 2007, ApJ, 664, L99
Phillips, T. R., Maluendes, S., & Green, S. 1996, ApJS, 107, 467
Poelman, D. R., & Spaans, M. 2005, A&A, 440, 559
Poelman, D. R., & van der Tak, F. F. S. 2007, A&A, 475, 949
Poglitsch, A., Waelkens, C., & Geis, N. 2001, in The Promise of the Herschel Space Observatory, ed. G. L. Pilbratt, J. Cernicharo, A. M. Heras, T. Prusti, & R. Harris, ESA SP-460, 29
Pontoppidan, K. M., van Dishoeck, E. F., & Dartois, E. 2004, A&A, 426, 925
Ristorcelli, I., Falgarone, E., Schöier, F., et al. 2005, in IAU Symp. 184, ed. D. C. Lis, G. A. Blake, & E. Herbst
Schöier, F. L., Jørgensen, J. K., van Dishoeck, E. F., & Blake, G. A. 2002, A&A, 390, 1001
Schöier, F. L., Jørgensen, J. K., van Dishoeck, E. F., & Blake, G. A. 2004, A&A, 418, 185
Schöier, F. L., van der Tak, F. F. S., van Dishoeck, E. F., & Black, J. H. 2005, A&A, 432, 369
Shirley, Y. L., Evans, N. J., Rawlings, J. M. C., & Gregersen, E. M. 2000, ApJS, 131, 249
Shu, F. H. 1977, ApJ, 214, 488
Smith, R. G., Sellgren, K., & Tokunaga, A. T. 1989, ApJ, 344, 413
Snell, R. L., Howe, J. E., Ashby, M. L. N., et al. 2000, ApJ, 539, L101
Stark, R., Sandell, G., Beck, S. C., et al. 2004, ApJ, 608, 341
Turner, B. E., Fourikis, N., Morris, M., Palmer, P., & Zuckerman, B. 1975, ApJ, 198, L125
van der Tak, F. F. S., van Dishoeck, E. F., Evans, N. J., & Blake, G. A. 2000, ApJ, 537, 283
van der Tak, F., Neufeld, D., Yates, J., et al. 2005, in ESA SP-577, ed. A. Wilson, 431
van der Tak, F. F. S., Walmsley, C. M., Herpin, F., & Ceccarelli, C. 2006, A&A, 447, 1011
van Dishoeck, E. F. 2003, in SFChem 2002: Chemistry as a Diagnostic of Star Formation, Proc. Conf. held August 21–23, 2002 at University of Waterloo, Ontario, Canada, ed. C. L. Curry, & M. Fich (Ottawa, Canada: NRC Press), 201
van Dishoeck, E. F., & Blake, G. A. 1998, ARA&A, 36, 317
van Dishoeck, E. F., Blake, G. A., Draine, B. T., & Lunine, J. I. 1993, in Protostars and Planets III, ed. E. H. Levy, & J. I. Lunine, 163
van Zadelhoff, G.-J., Dullemond, C. P., van der Tak, F. F. S., et al. 2002, A&A, 395, 373
Ward-Thompson, D., & Buckley, H. D. 2001, MNRAS, 327, 955
Watson, D. M., Bohac, C. J., Hull, C., et al. 2007, Nature, 448, 1026
Whittet, D. C. B., Bode, M. F., Baines, D. W. T., Longmore, A. J., & Evans, A. 1983, Nature, 303, 218
Wilson, T. L., & Rood, R. 1994, ARA&A, 32, 191
Young, C. H., & Evans, II, N. J. 2005, ApJ, 627, 293

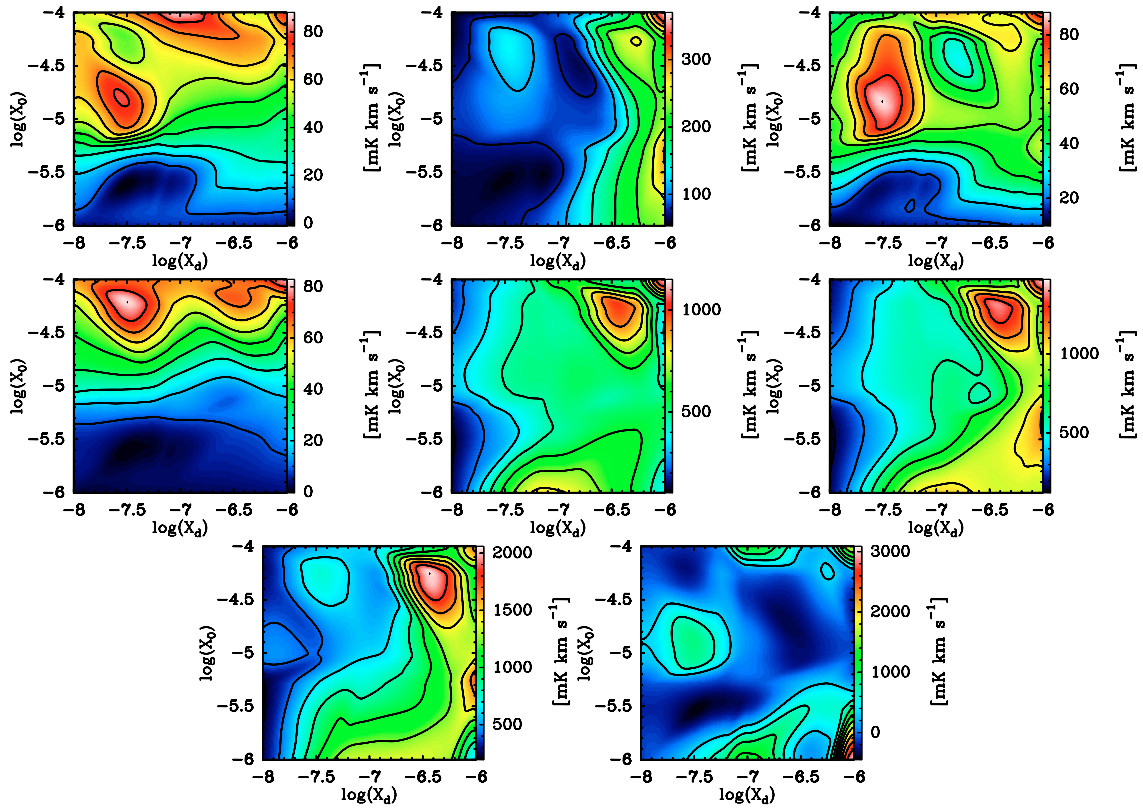

Fig. 11. Contour plots of the integrated intensity of the L 483 models as a function of inner (X_0) and outer (X_d for all para-H_2O lines. *Upper row* (*from left to right*): 5_{24}–4_{31}, 4_{22}–4_{13} and 4_{22}–3_{31}. *Middle row*: 3_{31}–4_{04}, 2_{20}–2_{11} and 2_{11}–2_{02}. *Lower row*: 2_{02}–1_{11} and 1_{11}–0_{00}.

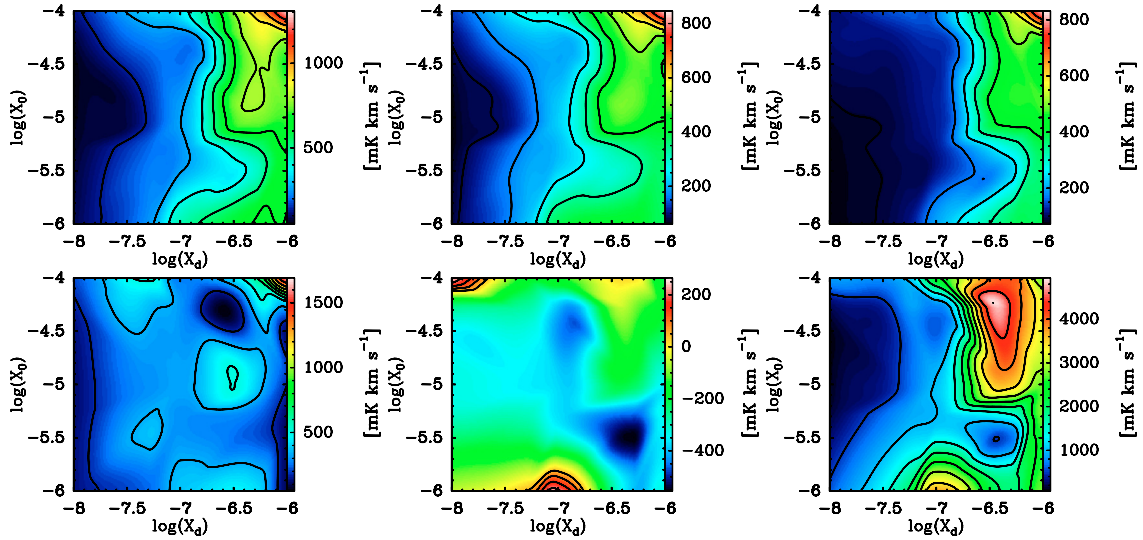

Fig. 12. Contour plots of the integrated intensity of the L 483 models as a function of inner (X_0) and outer (X_d for all ortho-H_2O lines. *Upper row* (*from left to right*): 3_{21}–3_{12}, 3_{12}–3_{03} and 3_{12}–2_{21}. *Lower row*: 2_{21}–2_{12}, 2_{12}–1_{01} and 1_{10}–1_{01}.

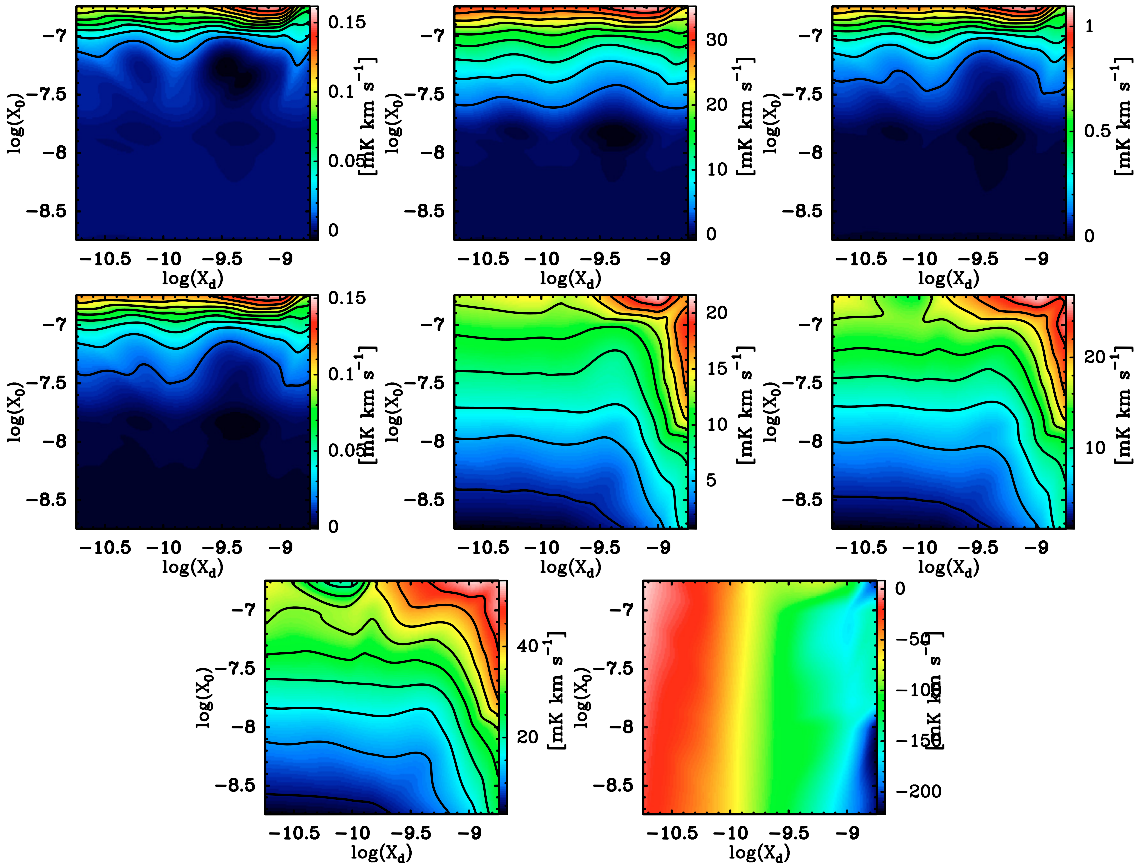

Fig. 13. Contour plots of the integrated intensity of the L 483 models as a function of inner (X_0) and outer (X_d for all para-$H_2^{18}O$ lines. *Upper row* (*from left to right*): 5_{24}–4_{31}, 4_{22}–4_{13} and 4_{22}–3_{31}. *Middle row*: 3_{31}–4_{04}, 2_{20}–2_{11} and 2_{11}–2_{02}. *Lower row*: 2_{02}–1_{11} and 1_{11}–0_{00}.

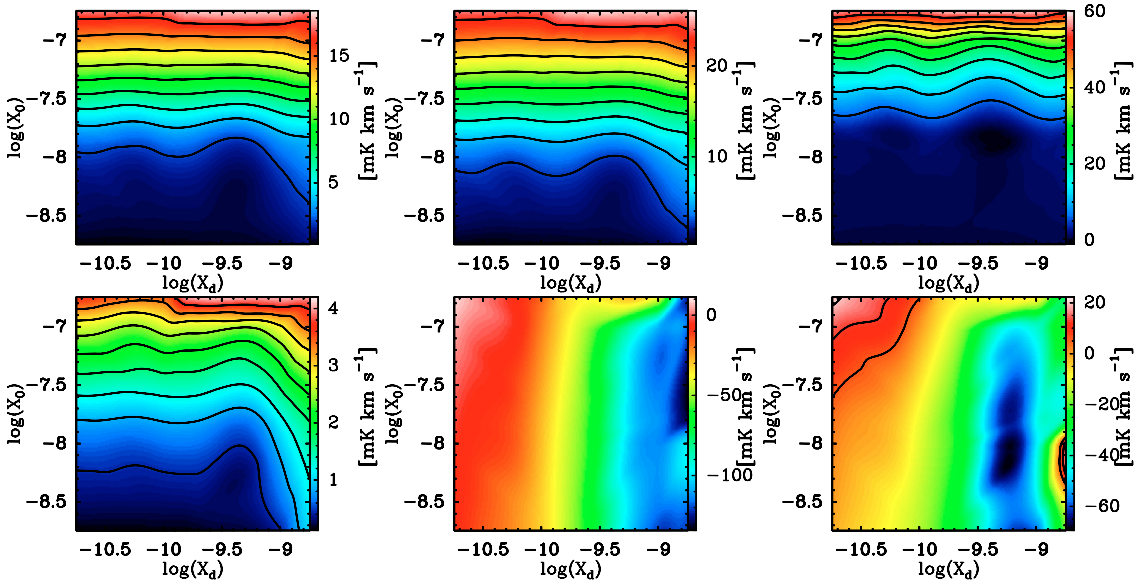

Fig. 14. Contour plots of the integrated intensity of the L 483 models as a function of inner (X_0) and outer (X_d for all ortho-$H_2^{18}O$ lines. *Upper row* (*from left to right*): 3_{21}–3_{12}, 3_{12}–3_{03} and 3_{12}–2_{21}. *Lower row*: 2_{21}–2_{12}, 2_{12}–1_{01} and 1_{10}–1_{01}.

Table 9. Integrated intensities, $\int T_{\rm MB}\Delta V$ [K km s^{-1}], for H_2O lines in the wide parameter grid for all abundances. Ortho lines for p = 1.5.

Density (cm^{-3})	Integrated intensity $\int T_{\rm MB}\Delta V$ [K km s^{-1}]																	
	L = 2($L_\odot$) Abundance[a]						L = 25($L_\odot$) Abundance[a]						L = 7($L_\odot$) Abundance[a]					
	1a	1b	1c	2a	2b	2c	1a	1b	1c	2a	2b	2c	1a	1b	1c	2a	2b	2c
									$1_{10}-1_{01}$									
4×10^5	0.68	0.27	4.7(–2)	2.1	0.18	6.2(–2)	1.2	0.55	0.27	1.3	0.23	0.14	4.1	0.43	0.12	0.59	0.19	9.1(–2)
1×10^6	2.7	2.7	0.37	0.24	2.9	0.64	0.16	6.2	0.70	0.48	2.2	0.54	0.29	2.5	0.95	0.17	1.8	0.56
5×10^6	3.6	2.3	0.22	3.9	2.1	1.7	11.2	1.9	0.33	15.0	2.0	0.16	8.6	2.1	0.22	3.6	3.9	0.43
									$2_{12}-1_{01}$									
4×10^5	2.9(–2)	7.2(–2)	-2.5(–2)	2.1	–1.3(–2)	4.2(–2)	0.26	0.82	0.92	0.11	-0.37	0.28	5.0	0.30	0.19	-0.24	–0.21	2.48(–3)
1×10^6	3.7	–0.35	3.6(–2)	1.2	–0.21	–0.17	1.0	–1.2	–0.14	–1.7	–1.7	–0.75	–0.43	–0.36	–0.54	–0.83	–0.80	0.88
5×10^6	–1.3	–1.1	–1.7	–1.4	–1.6	–3.6(–2)	–9.1	–9.1	–7.5	–5.5	–9.1	–7.7	–3.9	–4.4	–3.8	–3.9	–3.6	–3.7
									$2_{21}-2_{12}$									
4×10^5	0.20	0.51	0.16	0.40	0.17	7.4(–2)	1.4	1.2	1.2	0.73	0.67	0.65	1.2	0.60	0.45	0.41	0.32	0.17
1×10^6	4.8	0.29	0.25	0.13	0.42	0.14	6.3	1.5	1.6	0.42	1.2	0.67	2.3(–2)	0.87	0.46	0.20	0.55	0.38
5×10^6	–0.29	0.16	0.10	–0.59	–0.30	0.48	–5.1	–2.0	1.0	2.0	–2.0	0.42	–1.3	–0.74	0.50	–0.54	–0.69	0.29
									$3_{12}-3_{03}$									
4×10^5	0.26	0.18	8.3(–2)	0.32	0.11	5.8(–2)	2.0	1.1	0.91	1.7	0.75	0.77	0.95	0.38	0.25	0.65	0.26	0.18
1×10^6	0.82	0.21	9.1(–2)	0.37	0.22	6.9(–2)	8.3	1.5	0.92	3.1	1.3	0.69	1.1	0.60	0.25	1.3	0.47	0.23
5×10^6	0.57	0.32	6.9(–2)	0.69	0.28	8.8(–2)	4.3	2.7	0.92	4.1	2.5	0.77	1.9	0.89	0.23	0.98	0.95	0.23
									$3_{12}-2_{21}$									
4×10^5	0.19	0.19	8.3(–2)	0.31	0.10	5.2(–2)	1.5	1.1	0.70	1.4	0.69	0.44	0.83	0.40	0.24	0.47	0.26	0.14
1×10^6	0.93	0.21	0.12	0.33	0.23	9.2(–2)	5.8	1.6	1.1	2.1	1.4	0.69	0.78	0.67	0.29	0.71	0.50	0.30
5×10^6	0.37	0.37	0.12	0.33	0.30	0.18	2.4	2.9	1.5	3.3	2.5	1.3	1.1	0.84	0.42	1.0	0.99	0.42
									$3_{21}-3_{12}$									
4×10^5	0.328	0.302	0.103	0.575	0.155	5.604(–2)	2.84	1.4	0.753	2.67	0.929	0.672	1.52	0.592	0.308	0.867	0.372	0.152
1×10^6	1.44	0.317	0.16	0.633	0.372	0.118	12.1	2.69	1.28	4.49	2.29	0.832	1.53	1.09	0.374	1.59	0.824	0.398
5×10^6	0.785	0.609	0.157	0.809	0.547	0.236	7.34	5.44	2.28	9.35	5.17	2.05	2.8	1.64	0.60	1.96	1.85	0.612

[a] The abundance combinations are as follows: 1: $X_0 = 10^{-4}$, 2: $X_0 = 10^{-6}$ and a: $X_{\rm d} = 10^{-6}$, b: $X_d = 10^{-7}$, c: $X_{\rm d} = 10^{-8}$.
Note: $A(B) = A \times 10^{\rm B}$.

Table 10. Integrated intensities, $\int T_{\rm MB}\Delta V$ [K km s^{-1}], for H_2O lines in the wide parameter grid for all abundances, Ortho lines for p = 2.0.

Density (cm^{-3})	Integrated Intensity $\int T_{\rm MB}\Delta V$ [K km s^{-1}]																	
	L = 2 ($L_\odot$) Abundance[a]						L = 25 ($L_\odot$) Abundance[a]						L = 7 ($L_\odot$) Abundance[a]					
	1a	1b	1c	2a	2b	2c	1a	1b	1c	2a	2b	2c	1a	1b	1c	2a	2b	2c
									$1_{10}-1_{01}$									
4×10^5	0.37	5.1(–2)	0.23	1.2	5.1(–2)	0.11	0.45	0.28	0.25	0.63	0.25	0.19	1.5	0.10	0.20	1.6	0.69	0.11
1×10^6	2.4	2.4	0.12	0.19	1.1	0.27	0.11	2.8	0.19	0.41	0.85	0.19	0.28	2.8	0.24	0.11	3.3	0.16
5×10^6	4.0	2.2	0.36	5.0	1.7	0.59	14.0	1.6	–6.2(–2)	4.5	2.4	1.2	9.0	0.82	0.78	7.3	0.89	0.11
									$2_{12}-1_{01}$									
4×10^5	–0.27	–0.43	0.43	0.35	–0.43	–0.10	–0.98	–0.73	9.6(–2)	–0.68	–0.79	–0.11	0.27	–0.71	0.17	5.7(–2)	0.42	–0.31
1×10^6	–0.16	–0.89	–0.47	–0.53	–0.80	–0.62	–1.3	–3.08	–1.4	–3.2	–3.1	–1.8	–0.88	–1.6	–1.3	6.3(–3)	–1.7	–0.88
5×10^6	–1.1	–1.5	–1.9	–0.62	–2.1	–1.7	–7.2	–9.3	–8.4	–10.4	–8.7	–6.5	–3.2	–5.0	–3.6	–3.6	–4.9	–4.2
									$2_{21}-2_{12}$									
4×10^5	–0.11	–6.6(–3)	0.11	3.6(–2)	–1.4(–2)	6.3(–2)	0.47	0.94	0.91	0.22	0.77	0.46	0.57	0.13	0.20	1.2	0.55	0.17
1×10^6	–0.23	–0.13	6.2(–2)	–0.35	2.6(–2)	0.11	0.14	0.15	0.53	–0.95	1.9(–2)	0.41	0.28	0.14	0.20	–0.23	–0.13	0.18
5×10^6	–0.58	–0.58	8.5(–4)	–0.93	–0.7	5.6(–3)	–4.8	–3.07	–0.36	–6.3	–3.2	–1.1	–2.1	–1.4	–0.18	–1.0	–1.5	–0.11
									$3_{12}-3_{03}$									
4×10^5	0.23	0.13	6.3(–2)	0.25	0.13	5.2(–2)	2.0	1.1	0.70	1.6	0.98	0.54	0.88	0.35	0.20	1.1	0.43	0.16
1×10^6	0.31	0.12	4.6(–2)	0.29	0.16	4.7(–2)	2.9	1.3	0.63	2.6	1.2	0.53	1.2	0.47	0.15	0.85	0.39	0.15
5×10^6	0.19	0.15	2.9(–2)	0.18	0.16	3.2(–2)	2.4	1.9	0.44	3.1	1.9	0.56	0.78	0.51	0.14	1.06	0.47	0.13
									$3_{12}-2_{21}$									
4×10^5	0.18	9.3(–2)	8.9(–2)	0.19	8.1(–2)	7.1(–2)	1.18	0.99	0.73	1.2	0.97	0.53	0.69	0.29	0.23	0.83	0.46	0.19
1×10^6	0.20	0.13	7.3(–2)	0.21	0.16	6.8(–2)	2.1	1.2	0.86	1.4	1.1	0.73	0.80	0.48	0.20	0.73	0.40	0.23
5×10^6	0.20	0.14	6.7(–2)	0.15	0.11	7.3(–2)	2.7	1.6	0.80	0.89	1.8	0.98	0.48	0.49	0.28	0.76	0.55	0.24
									$3_{21}-3_{12}$									
4×10^5	0.29	0.14	0.13	0.35	0.13	0.10	2.3	1.6	0.93	2.4	1.6	0.65	1.3	0.45	0.33	1.6	0.77	0.26
1×10^6	0.45	0.20	0.11	0.41	0.27	0.10	4.4	2.1	1.2	3.4	2.0	1.1	1.6	0.87	0.30	1.5	0.73	0.35
5×10^6	0.49	0.35	0.11	0.48	0.33	0.1	6.3	4.0	1.5	4.9	4.3	1.8	1.7	1.2	0.49	1.9	1.3	0.43

[a] The abundance combinations are as follows: 1: $X_0 = 10^{-4}$, 2: $X_0 = 10^{-6}$ and a: $X_{\rm d} = 10^{-6}$, b: $X_{\rm d} = 10^{-7}$, c: $X_{\rm d} = 10^{-8}$.
Note: $A(B) = {\rm A}\times10^{\rm B}$.

Table 11. Integrated intensities, $\int T_{\rm MB}\Delta V$ [K km s^{-1}], for H_2O lines in the wide parameter grid for all abundances. Para lines for $p = 1.5$.

Density (cm^{-3})	Integrated intensity $\int T_{\rm MB}\Delta V$ [K km s^{-1}]																	
	$L = 2$ ($L_\odot$) Abundance[a]						$L = 25$ ($L_\odot$) Abundance[a]						$L = 7$ ($L_\odot$) Abundance[a]					
	1a	1b	1c	2a	2b	2c	1a	1b	1c	2a	2b	2c	1a	1b	1c	2a	2b	2c
									1_{11}–0_{00}									
4×10^5	0.50	0.23	9.0(–2)	3.0	0.22	6.9(–2)	1.4	0.52	0.48	2.8	0.20	0.14	0.64	0.43	0.18	1.0	0.26	9.4(–2)
1×10^6	1.0	1.0	0.13	0.15	0.62	0.38	0.13	1.5	0.31	0.28	1.2	1.2	4.7(–2)	1.5	1.0	0.19	2.9	5.4(–3)
5×10^6	1.5	–1.6(–2)	4.0(–2)	1.9	0.19	0.22	–0.45	–1.8	–0.70	6.2	–1.1	–2.3	0.88	1.6	–0.66	3.1	0.9	–0.55
									2_{02}–1_{11}									
4×10^5	0.65	0.32	0.12	3.8	0.31	9.0(–2)	3.2	1.6	0.87	2.8	1.2	0.43	1.2	0.72	0.28	1.3	0.62	0.19
1×10^6	1.3	0.58	0.24	1.0	0.64	0.22	6.7	3.0	1.3	3.9	3.1	0.99	2.0	1.5	0.53	1.7	1.2	0.46
5×10^6	1.7	0.76	0.60	1.6	0.82	0.6	6.8	5.2	4.3	15.1	4.6	4.2	5.1	1.1	1.9	3.4	1.1	1.9
									2_{11}–2_{02}									
4×10^5	0.37	0.17	6.2(–2)	1.4	0.17	4.8(–2)	2.3	1.0	0.51	2.4	0.78	0.26	0.78	0.41	0.16	0.87	0.36	1.0(–1)
1×10^6	0.75	0.34	0.13	0.60	0.39	0.12	4.9	2.0	0.79	3.5	2.4	0.62	1.5	1.0	0.29	1.4	0.72	0.26
5×10^6	1.3	0.82	0.47	1.4	0.85	0.48	10.4	6.5	5.0	25.7	6.8	4.4	4.9	2.7	1.8	3.9	2.3	1.8
									2_{20}–2_{11}									
4×10^5	0.31	0.18	8.8(–2)	1.1	0.15	4.7(–2)	2.3	1.1	0.69	2.2	0.74	0.22	0.70	0.47	0.18	0.79	0.34	9.4(–2)
1×10^6	0.62	0.31	0.13	0.38	0.34	0.11	4.7	2.3	0.94	3.0	2.3	0.59	1.2	1.0	0.36	1.1	0.69	0.25
5×10^6	0.37	0.45	0.33	0.44	0.47	0.33	3.9	4.1	4.3	16.8	4.5	3.8	1.4	1.4	1.4	2.7	1.3	1.4
									3_{31}–4_{04}									
4×10^5	5.9(–2)	5.8(–2)	5.7(–2)	4.6(–3)	1.8(–3)	1.7(–3)	0.57	0.56	0.56	1.4(–2)	8.0(–3)	7.6(–3)	0.18	0.18	0.18	7.4(–3)	4.0(–3)	3.8(–3)
1×10^6	4.7(–2)	4.2(–2)	4.1(–2)	7.4(–3)	3.8(–3)	3.4(–3)	0.60	0.58	0.58	4.7(–2)	2.6(–2)	2.6(–2)	0.16	0.15	0.15	1.8(–2)	1.0(–2)	9.8(–3)
5×10^6	1.1(–3)	–7.8(–4)	–9.6(–4)	2.6(–3)	6.8(–4)	5.0(–4)	0.20	8.1(–2)	6.9(–2)	0.2	6.9(–2)	5.5(–2)	2.9(–2)	1.3(–3)	–1.5(–3)	3.6(–2)	9.6(–3)	7.6(–3)
									4_{22}–3_{31}									
4×10^5	4.8(–2)	4.2(–2)	4.2(–2)	2.2(–2)	1.0(–2)	9.8(–3)	0.56	0.56	0.56	9.7(–2)	6.2(–2)	6.0(–2)	0.15	0.13	0.13	4.4(–2)	2.8(–2)	2.7(–2)
1×10^6	4.9(–2)	4.1(–2)	4.3(–2)	3.1(–2)	1.7(–2)	1.6(–2)	0.59	0.48	0.47	0.27	0.18	0.17	0.16	0.13	0.12	9.0(–2)	5.6(–2)	5.3(–2)
5×10^6	4.0(–2)	1.9(–2)	1.5(–2)	3.5(–2)	1.4(–2)	1.1(–2)	0.87	0.39	0.31	0.78	0.31	0.23	0.22	9.6(–2)	6.8(–2)	0.19	8.0(–2)	5.2(–2)
									4_{22}–4_{13}									
4×10^5	0.15	6.6(–2)	5.1(–2)	0.18	5.7(–2)	4.5(–2)	1.0	0.64	0.63	1.1	0.54	0.51	0.37	0.18	0.15	0.39	0.17	0.15
1×10^6	0.20	9.5(–2)	5.1(–2)	0.19	8.4(–2)	4.3(–2)	2.2	0.74	0.55	2.0	0.75	0.60	0.58	0.26	0.15	0.53	0.24	0.15
5×10^6	0.14	6.6(–2)	2.3(–2)	0.13	6.4(–2)	2.1(–2)	3.4	1.8	0.66	3.4	1.8	0.60	0.86	0.41	0.15	0.87	0.41	0.15
									5_{24}–4_{31}									
$4{\times}10^5$	5.0(–2)	5.0(–2)	5.0(–2)	6.7(–3)	6.6(–3)	0.59	0.61	0.62	3.6(–2)	2.6(–2)	2.7(–2)	0.16	0.16	0.16	2.0(–2)	1.6(–2)	1.5(–2)	4.3(–2)
1×10^6	5.0(–2)	5.0(–2)	5.1(–2)	1.9(–2)	1.4(–2)	1.4(–2)	0.58	0.57	0.57	0.14	0.12	0.12	0.17	0.15	0.15	5.2(–2)	4.3(–2)	4.3(–2)
5×10^6	2.6(–2)	1.8(–2)	2.0(–2)	1.2(–2)	1.1(–2)	0.54	0.39	0.37	0.43	0.27	0.25	0.14	8.8(–2)	7.9(–2)	0.12	6.3(–2)	5.6(–2)	4.3(–2)

[a] The abundance combinations are as follows: **1:** $X_0 = 10^{-4}$, **2:** $X_0 = 10^{-6}$ and a: $X_{\rm d} = 10^{-6}$, b: $X_{\rm d} = 10^{-7}$, c: $X_{\rm d} = 10^{-8}$.
Note: $A(B) = A \times 10^{\rm B}$

Table 12. Integrated intensities, $\int T_{\rm MB}\Delta V$ [K km s^{-1}], for H_2O lines in the wide parameter grid for all abundances for para $p = 2.0$.

Density (cm^{-3})	Integrated intensity $\int T_{\rm MB}\Delta V$ [K km s^{-1}]																	
	$L = 2$ ($L_\odot$) Abundance[a]						$L = 25$($L_\odot$) Abundance[a]						$L = 7$ ($L_\odot$) Abundance[a]					
	1a	1b	1c	2a	2b	2c	1a	1b	1c	2a	2b	2c	1a	1b	1c	2a	2b	2c
									1_{11}–0_{00}									
4×10^5	3.9	0.11	9.3(–2)	0.51	0.26	8.4(–2)	0.7	0.43	0.38	2.8	0.24	0.22	0.29	0.52	0.15	1.4	0.17	0.12
1×10^6	0.34	0.34	0.30	0.10	0.71	0.30	0.12	0.44	0.23	8.1(–2)	0.21	–0.11	3.6(–3)	0.66	9.4(–2)	8.3(–2)	1.6	2.7
5×10^6	1.7	0.98	–0.26	0.91	0.44	–0.10	–1.9	2.0	–1.8	–3.5	0.16	–2.1	–0.2	–9.0(–2)	–0.18	6.1	–0.49	–0.57
									2_{02}–1_{11}									
4×10^5	2.9	0.40	0.18	0.76	0.4	0.18	2.8	1.9	0.95	2.9	1.7	0.74	1.2	0.90	0.40	1.9	0.8	0.35
1×10^6	0.90	0.66	0.31	0.86	0.65	0.29	4.1	3.1	1.6	3.6	2.8	1.5	1.9	1.4	0.65	1.8	1.6	0.62
5×10^6	1.4	0.94	0.46	1.36	0.68	0.47	2.2	3.8	2.7	7.6	3.57	2.6	0.77	1.8	1.1	5.5	1.6	1.2
									2_{11}–2_{02}									
4×10^5	1.3	0.24	9.8(–2)	0.46	0.26	9.4(–2)	1.9	1.1	0.54	2.2	1.0	0.43	0.79	0.56	0.21	1.16	0.49	0.19
1×10^6	0.66	0.46	0.19	0.66	0.45	0.19	3.0	2.1	0.89	2.8	1.9	0.83	1.4	0.94	0.40	1.5	1.2	0.38
5×10^6	1.4	0.99	0.45	1.3	0.88	0.47	4.7	5.9	2.5	6.1	5.2	2.4	1.9	2.2	1.1	4.7	2.1	1.1
									2_{20}–2_{11}									
4×10^5	1.1	0.19	8.6(–2)	0.31	0.21	8.1(–2)	1.8	1.3	0.75	2.1	1.1	0.4	0.58	0.54	0.24	1.0	0.47	0.18
1×10^6	0.30	0.32	0.13	0.34	0.32	0.13	2.5	2.1	0.96	1.9	1.8	0.81	0.93	0.78	0.33	1.1	1.0	0.31
5×10^6	0.50	0.50	0.25	0.26	0.43	0.26	1.2	4.1	1.9	1.8	3.5	1.9	0.18	1.3	0.75	2.6	1.2	0.74
									3_{31}–4_{04}									
4×10^5	8.4(–3)	5.5(–3)	5.0(–3)	5.8(–3)	2.6(–3)	2.3(–3)	0.46	0.45	0.42	5.7(–2)	4.0(–2)	3.8(–2)	7.9(–2)	7.1(–2)	7.0(–2)	2.2(–2)	1.3(–2)	1.2(–2)
1×10^6	–1.8(–3)	–3.7(–3)	–3.9(–3)	1.6(–3)	1.1(–5)	–1.6(–4)	0.16	0.13	0.13	6.4(–2)	3.9(–2)	3.6(–2)	1.6(–3)	–6.7(–3)	–7.3(–3)	1.3(–2)	4.5(–3)	3.5(–3)
5×10^6	–2.5(–4)	–3.2(–5)	–1.1(–5)	–2.9(–4)	–2.5(–5)	–2.6(–6)	–1.7(–2)	–3.0(–2)	–3.1(–2)	8.6(–3)	–2.3(–3)	–3.3(–3)	–1.5(–3)	–1.2(–3)	–1.2(–3)	2.4(–4)	–1.9(–4)	–1.7(–4)
									4_{22}–3_{31}									
4×10^5	3.7(–2)	2.2(–2)	2.0(–2)	2.9(–2)	1.5(–2)	1.3(–2)	0.44	0.40	0.43	0.26	0.20	0.19	0.12	9.3(–2)	9.2(–2)	9.1(–2)	5.7(–2)	5.4(–2)
1×10^6	2.7(–2)	1.0(–2)	7.2(–3)	2.5(–2)	9.1(–3)	6.0(–3)	0.41	0.31	0.29	0.30	0.20	0.19	0.11	5.9(–2)	5.2(–2)	9.2(–2)	4.6(–2)	3.8(–2)
5×10^6	5.7(–3)	3.0(–4)	–8.6(–4)	6.0(–3)	7.3(–4)	–3.9(–4)	0.24	5.2(–2)	1.9(–2)	0.25	6.0(–2)	2.8(–2)	3.3(–2)	2.3(–3)	–5.5(–3)	3.8(–2)	6.1(–3)	–1.5(–3)
									4_{22}–4_{13}									
4×10^5	0.14	6.8(–2)	2.8(–2)	0.13	6.3(–2)	2.4(–2)	1.4	0.61	0.42	1.4	0.60	0.49	0.40	0.22	0.12	0.40	0.21	0.11
1×10^6	0.10	4.7(–2)	1.2(–2)	0.10	4.7(–2)	1.2(–2)	1.8	0.74	0.35	1.7	0.69	0.34	0.42	0.19	7.0(–2)	0.43	0.19	6.4(–2)
5×10^6	4.2(–2)	8.5(–3)	1.1(–3)	4.16(–2)	8.6(–3)	1.2(–3)	1.5	0.55	7.1(–2)	1.4	0.56	8.6(–2)	0.32	8.0(–2)	7.8(–3)	0.31	8.3(–2)	1.0(–2)
									5_{24}–4_{31}									
4×10^5	3.1(–2)	2.6(–2)	2.6(–2)	2.0(–2)	1.5(–2)	1.4(–2)	0.50	0.49	0.51	0.19	0.17	0.16	0.13	0.12	0.12	6.7(–2)	5.5(–2)	5.4(–2)
1×10^6	1.5(–2)	8.3(–3)	7.6(–3)	1.3(–2)	7.0(–3)	6.2(–3)	0.40	0.34	0.35	0.23	0.19	0.19	8.2(–2)	6.5(–2)	6.2(–2)	6.3(–2)	4.3(–2)	4.1(–2)
5×10^6	–9.9(–5)	–9.4(–4)	–1.1(–3)	3.3(–4)	–3.7(–4)	–4.9(–4)	6.0(–2)	1.3(–2)	7.5(–3)	7.7(–2)	3.0(–2)	2.4(–2)	2.3(–3)	–6.9(–3)	–8.7(–3)	7.8(–3)	–1.0(–3)	–2.6(–3)

[a] The abundance combinations are as follows: 1: $X_0 = 10^{-4}$, 2: $X_0 = 10^{-6}$ and a: $X_{\rm d} = 10^{-6}$, b: $X_{\rm d} = 10^{-7}$, c: $X_{\rm d} = 10^{-8}$.
Note: $A(B)$ denotes $A \times 10^B$.